

# Analysis of finite-volume discrete adjoint fields for two-dimensional compressible Euler flows

Jacques Peter<sup>a,\*</sup>, Florent Renac<sup>a</sup>, Clément Labbé<sup>a</sup>

<sup>a</sup>DAAA, ONERA, Université Paris Saclay, F-92322 Châtillon, France

---

## Abstract

This work deals with a number of questions relative to the discrete and continuous adjoint fields associated to Euler equations and classical aerodynamic functions. The consistency of the discrete adjoint equations with the corresponding continuous adjoint partial differential equation is one of them. It has been established or at least discussed only for a handful of numerical schemes and a contribution of this article is to give the adjoint consistency conditions for the 2D Jameson-Schmidt-Turkel scheme in cell-centred finite-volume formulation. The consistency issue is also studied here from a new heuristic point of view by discretizing the continuous adjoint equation for the discrete flow and adjoint fields. Both points of view prove to provide useful information. Besides, it has been often noted that discrete or continuous inviscid lift and drag adjoint exhibit numerical divergence close to the wall and stagnation streamline for a wide range of subsonic and transonic flow conditions. This is analyzed here using the physical source term perturbation method introduced in reference [1]. With this point of view, the fourth physical source term of [1] appears to be the only one responsible for this behavior. It is also demonstrated that the numerical divergence of the adjoint variables corresponds to the response of the flow to the convected increment of stagnation pressure and diminution of entropy created at the source and the resulting change in lift and drag.

*Keywords:* discrete adjoint method, continuous adjoint method, dual consistency, adjoint Rankine-Hugoniot, compressible Euler equations

---

## 1. Introduction

Discrete and continuous adjoint methods are well established methods to efficiently calculate derivatives of aerodynamic functions with respect to numerous design parameters. Adjoint-based derivatives and adjoint-fields are commonly used for local shape optimization [2, 3, 4, 5, 6], goal-oriented mesh adaptation [7, 8, 9, 10, 11, 12, 13, 14], and also other fields like flow control [15, 16], meta-modelling [17], receptivity-sensitivity-stability analyses [18] and data assimilation [19]. These methods are often used for the linear analysis of non-linear conservation laws where the adjoint is defined as the dual to the linearized equations around a given solution to the direct non-linear problem. The continuous adjoint method refers to the discretization of the adjoint equations associated to the formal direct problem, while the discrete adjoint method refers to the adjoint equations to the discrete direct problem.

Concerning the discrete adjoint method, strong efforts have been devoted to implement (either by hand or using automatic differentiation) the exact linearization of complex schemes for complex models [20, 21] and also to enhance the robustness of the linear solver [22, 23] whereas fundamental questions relative to discrete adjoint fields are still open even for two-dimensional (2D) compressible Euler flows. Numerical simulations including viscous laminar and turbulent effects are today common practices in CFD. It is nevertheless desirable to gain understanding in the discrete adjoint method addressing unresolved issues in the framework of 2D Euler equations.

First, are the discrete adjoint fields consistent with the continuous equation at the limit of fine meshes? This question goes back to a discussion by Giles et al. in [24] where the authors discuss the discrete adjoint counterpart of a

---

\*Corresponding author. Tel.: +33 1 46 73 41 84.

Email addresses: [jacques.peter@onera.fr](mailto:jacques.peter@onera.fr) (Jacques Peter), [florent.renac@onera.fr](mailto:florent.renac@onera.fr) (Florent Renac)

strong boundary condition at a wall and derive a normal projection of the momentum adjoint variable that does not correspond to the normal momentum component of the continuous adjoint solution at the boundary. This of course raises the question which schemes are adjoint-consistent and which are not, and what are the consequences of the lack of dual-consistency. These questions have been studied in a handful of articles where the authors have first to precisely describe the numerical method they consider, including the possibly specific discretization close to the boundary, and also the way the function of interest is discretized. Lu and Darmofal [25] considered a discontinuous Galerkin (DG) scheme and then demonstrated how to formulate the primal boundary condition and the output functional to obtain dual-consistency. The difference between the consistent and non-consistent formulations is noticed in both the appearance of the adjoint contours close to the function support and the convergence rate of the output of interest w.r.t. the characteristic mesh size. Hartmann [26] also discussed dual consistency for DG schemes, including interior penalty DG and also dealt with Navier-Stokes equations and test-cases. The adjoint consistency of a high-order correction procedure via reconstruction formulation for hyperbolic conservation laws was investigated in [27]. As concerning finite-differences and finite-volume (FV), the questions of adjoint-consistency was discussed by Duivesteyn et al. and Lozano for quasi 1D Euler flows [28, 29] and also for an unsteady conservation law by Liu and Sandu [30]. In this later article, the authors considered first-order and second-order upwind schemes and derived the circumstances in which the discrete adjoint is punctually not consistent (change of convection direction, inadequate discretization of boundary condition in particular). Hicken and Zingg have demonstrated the influence of adjoint consistency for a class of summation-by-parts difference schemes, illustrating the benefit of consistency in terms of regularity of adjoint contours close to boundaries, functional mesh convergence and dual-weighted corrected functional mesh convergence [31]. Recently Stück carried out a corresponding effort for cell-vertex FV discretization (using median dual grids), deriving the condition on the output of interest and scheme residual for dual-consistency [32, 33]. In this article, the conditions for dual consistency of the classical Jameson-Schmidt-Turkel (JST) scheme in 2D cell-centered FV are derived. Besides, the dual consistency is also studied here from a heuristic point of view, discretizing the continuous adjoint equation for the discrete adjoint fields which adds valuable information to the theoretical study where the flow or the gradient of the adjoint is discontinuous and where numerical divergence of the adjoint is observed.

Then, in the case of hyperbolic equations, the validity of the adjoint linearization around discontinuities in the direct solution has to be carefully handled because it results in linear equations with discontinuous coefficients. The analysis must include the linearization of the jump relations at the discontinuity [34] which leads to a so-called interior boundary condition for the adjoint variables [35]. The adjoint relations to the Rankine-Hugoniot (RH) relations have been derived in [36] for the quasi-one-dimensional and in [37, 38] for the 2D compressible Euler equations and proved continuity of the adjoint variables across the shock. In contrast, their derivatives may be discontinuous [36, 1, 37]. Lozano [38] also briefly discussed the consistency of the continuous adjoint fields but on rather coarse meshes. The conclusions of his work leave the question open whether these relations are actually satisfied at the limit of fine discrete adjoint fields.

Finally, it has been well-documented [1, 39, 38, 40] that, at certain flow conditions, the inviscid lift and drag adjoint fields may exhibit increasing values as the mesh is refined close to the stagnation streamline, the wall and, for (at least locally) supersonic flows, the Mach lines impacting a shock foot. (An interested reader may also consider the same problem for a 2D potential flow [41, 40].) In the case of the stagnation line, Giles and Pierce derived a  $1/\sqrt{d}$  law for lift and drag adjoint [1] ( $d$  being the distance to the line), but they used the potential flow theory and this  $1/\sqrt{d}$  behaviour is not always well-observed for compressible flows [39, 38]. In an effort to analyse the zones of singular behavior, Todarello et al. [42] used the characterization of the discrete adjoint and looked how the flow is perturbed by a residual perturbation located in one of the these specific areas. This method is used again here but with perturbations of the residual corresponding to physical source terms [1] which allows fluid mechanics analysis. In this framework, it appears that the numerical divergence of the adjoint variables is due to the influence of the fourth of the source term proposed in [1], the corresponding convected increment of stagnation pressure and diminution of entropy (created at the source location) and the resulting change in lift and drag. Finally, another aspect of lift and drag 2D inviscid adjoint field is studied in details: in the case of a supersonic flow with detached shock wave, the structure of the adjoint field is theoretically derived in the constant flow area and the consistency of fine grid numerical solutions with this analytical model is checked.

The paper is organized as follows. Sections 2 and 3 are devoted to reminders about continuous and discrete adjoint solutions for Euler flows. The adjoint consistency of the cell-centered JST scheme with structured 2D meshes [43] is discussed in § 4. Section 5 presents the adjoint RH equations for Euler flows. The theoretical results about adjoint

consistency and adjoint-gradient discontinuity at shock waves are then assessed in § 6 using fine grid lift- and drag-adjoint fields for inviscid flows around the NACA0012 airfoil in supersonic (§ 6.1), transonic (§ 6.2) and subsonic (§ 6.3) regimes. In these sections, the question of the asymptotic behavior of adjoint at the wall/stagnation line and more generally high gradient/high-values in the adjoint fields is also discussed using Giles and Pierce physical source term approach derived in § 3.3. Finally, concluding remarks about this work are given in § 7.

## 2. Continuous adjoint equations for 2D Euler flows

The continuous adjoint equations for compressible flows were first derived by Jameson [4] in the case of a 2D Euler flow about a profile. He considered a body fitted structured grid that was mapped to a conformal rectangle and used the Euler equations in the resulting  $(\xi, \eta)$ -coordinates. A parametrization of the mapping then allowed to vary the airfoil shape in the physical space (without altering the domain of variation of the transformed coordinates) and to define a gradient calculation problem for functional outputs. The adjoint were also derived in [44, 36, 38, 37] using a framework including the linearization of the RH relations.

As, in this formulation, the system of transformed coordinates is attached to a structured mesh, the aforementioned equations could not be used for unstructured CFD for which a formulation in physical coordinates was necessary. The corresponding system of equations was first derived by Anderson and Venkatakrishnan in [45] (and one year later by Hiernaux and Essers [46, 47]). A slightly simplified presentation of the theoretical part of reference [45] is given below.

The quantity of interest is assumed to be the projection of the force applied by the fluid onto the solid, projected in the direction  $\bar{d} = (-\cos \alpha, \sin \alpha)^T$  for the lift, or  $\bar{d} = (\sin \alpha, \cos \alpha)^T$  for drag with  $\alpha$  the angle of attack:

$$J = \int_{\Gamma_w} p(\bar{n} \cdot \bar{d}) ds, \quad (1)$$

where  $\Gamma_w$  is the boundary of the solid body,  $\bar{n} = (n_x, n_y)^T$  is the local normal (external for fluid and internal for the solid) and  $p$  is the static pressure.

The 2D compressible Euler equations in conservative form read

$$\frac{\partial F_x(W)}{\partial x} + \frac{\partial F_y(W)}{\partial y} = 0 \quad \text{in } \Omega, \quad (2)$$

$W$  being the vector of conservative variables and  $F_x$  and  $F_y$  the physical fluxes,

$$W = \begin{pmatrix} \rho \\ \rho u_x \\ \rho u_y \\ \rho E \end{pmatrix}, \quad F_x(W) = \begin{pmatrix} \rho u_x \\ \rho u_x^2 + p \\ \rho u_x u_y \\ \rho u_x H \end{pmatrix}, \quad F_y(W) = \begin{pmatrix} \rho u_y \\ \rho u_x u_y \\ \rho u_y^2 + p \\ \rho u_y H \end{pmatrix},$$

with  $H = E + p/\rho$  the total specific enthalpy. We consider an ideal gas law for the static pressure  $p = (\gamma - 1)\rho e = (\gamma - 1)(\rho E - \frac{1}{2}\rho \|\bar{U}\|^2)$ , with  $\gamma$  the ratio of specific heats and  $\bar{U} = (u_x, u_y)^T$  the velocity vector. Let  $\delta W$  be a perturbation in the steady state flow that is caused by an infinitesimal perturbation of airfoil shape or flow conditions. As  $W$  and  $W + \delta W$  are solutions of the steady Euler equations for initial and perturbed problem, by difference we get

$$\frac{\partial(A\delta W)}{\partial x} + \frac{\partial(B\delta W)}{\partial y} = 0 \quad \text{in } \Omega,$$

with  $A$  and  $B$  the Jacobians of the fluxes  $F_x$  and  $F_y$ , respectively. The perturbation in  $J$  can be augmented by the dot product of above equation with an arbitrary co-state field  $\psi$

$$\delta J = \int_{\Gamma_w} \delta p(\bar{n} \cdot \bar{d}) ds + \int_{\Gamma_w} p(\delta(\bar{n}) \cdot \bar{d}) ds + \int_{\Gamma_w} p(\bar{n} \cdot \bar{d}) \delta(ds) + \int_{\Omega} \psi^T \left( \frac{\partial(A\delta W)}{\partial x} + \frac{\partial(B\delta W)}{\partial y} \right) dv.$$

Assuming smooth direct and adjoint solutions, the last term can be transformed by integration by parts into

$$- \int_{\Omega} \left( \frac{\partial \psi^T}{\partial x} A + \frac{\partial \psi^T}{\partial y} B \right) \delta W dv + \int_{\Gamma_w} \psi^T (n_x A + n_y B) \delta W ds + \int_{\Gamma_\infty} \psi^T (n_x A + n_y B) \delta W ds,$$

with  $\Gamma_\infty$  the farfield boundary. The perturbation in the objective may then be rewritten as

$$\begin{aligned} \delta J = & \int_{\Gamma_w} \delta p(\bar{n} \cdot \bar{d}) ds + \int_{\Gamma_w} p(\delta(\bar{n}) \cdot \bar{d}) ds + \int_{\Gamma_w} p(\bar{n} \cdot \bar{d}) \delta(ds) \\ & - \int_{\Omega} \left( \frac{\partial \psi^T}{\partial x} A + \frac{\partial \psi^T}{\partial y} B \right) \delta W dv + \int_{\Gamma_w} \psi^T (n_x A + n_y B) \delta W ds + \int_{\Gamma_\infty} \psi^T (n_x A + n_y B) \delta W ds \end{aligned} \quad (3)$$

The adjoint method removes the dependency in the flow perturbation  $\delta W$  for the calculation of the variation of  $J$ . This directly yields the adjoint equation in the fluid domain

$$-A^T \frac{\partial \psi}{\partial x} - B^T \frac{\partial \psi}{\partial y} = 0, \quad \text{in } \Omega. \quad (4)$$

Note that the last equation in (4) reads

$$\bar{U} \cdot \nabla \psi_1 - H \bar{U} \cdot \nabla \psi_4 = 0. \quad (5)$$

Besides the wall boundary condition on  $\Gamma_w$  links  $\delta \bar{n}$  and  $\delta W$  :

$$\delta(\bar{U} \cdot \bar{n}) = \delta(\bar{U}) \cdot \bar{n} + \bar{U} \cdot \delta(\bar{n}) = 0$$

so that the second and third components of  $\delta W$  satisfy

$$\delta W_2 n_x + \delta W_3 n_y + W_2 \delta n_x + W_3 \delta n_y = 0. \quad (6)$$

The explicit calculation of  $\psi^T (n_x A + n_y B) \delta W$  at the wall yields

$$\begin{aligned} \psi^T (n_x A + n_y B) \delta W = & (n_x \psi_2 + n_y \psi_3) \left( (\gamma - 1) \frac{\|\bar{U}\|^2}{2}, (1 - \gamma) u_x, (1 - \gamma) u_y, (\gamma - 1) \right) \begin{pmatrix} \delta W_1 \\ \delta W_2 \\ \delta W_3 \\ \delta W_4 \end{pmatrix} \\ & + (\psi_1 + u \psi_2 + v \psi_3 + H) (n_x \delta W_2 + n_y \delta W_3) \end{aligned}$$

where the first term of the right-hand-side accounts for the differentiated pressure term of Euler flux and the second term for the differentiated convective part of Euler flux. The last term is reformulated using the linearized boundary condition (6) then the sum of the terms involving the flow variation  $\delta W$  in the integrals over  $\Gamma_w$  is set to zero to define the adjoint wall boundary condition

$$(\bar{n} \cdot \bar{d}) \frac{dp}{dW} \delta W + (n_x \psi_2 + n_y \psi_3) \left( (\gamma - 1) \frac{\|\bar{U}\|^2}{2}, (1 - \gamma) u_x, (1 - \gamma) u_y, (\gamma - 1) \right) \begin{pmatrix} \delta W_1 \\ \delta W_2 \\ \delta W_3 \\ \delta W_4 \end{pmatrix} = 0. \quad (7)$$

The last term of (7) corresponds to the derivative of the static pressure with respect to  $W$ , so that the final and classical form of the boundary condition is simply

$$\bar{n} \cdot \bar{d} + \psi_2 n_x + \psi_3 n_y = 0. \quad (8)$$

In the farfield, no variation of the boundary needs to be considered. The Jacobian in direction  $\bar{n}$  can be rewritten by using a locally one dimensional characteristic decomposition to yield

$$\int_{\Gamma_\infty} \psi^T (n_x A + n_y B) \delta W ds = \int_{\Gamma_\infty} (\psi^T P^{-1} D P \delta W) ds. \quad (9)$$

It is assumed that  $P \delta W \simeq \delta(PW)$ . The variation in these characteristic variables is zero for the components corresponding to negative eigenvalues of the Jacobian,  $n_x A + n_y B$ , in the classical 1D approximate linearization at the boundary (information coming from outside of the domain and fixed characteristic value). The farfield adjoint BC simply imposes that the other component of  $\psi^T P^{-1}$  are zero so that  $\delta W^T (n_x A^T + n_y B^T) \psi$  vanishes for all  $\delta W$ .

### 3. Discrete adjoint equations

#### 3.1. Discrete gradient calculation

The finite volume scheme of interest defines the steady-state discrete flow vector  $W$  (of size  $n_W$ ) as the solution of a set of  $n_W$  non-linear equations involving  $W$  and the vector of mesh coordinates  $X$ :

$$R(W, X) = 0.$$

Let us assume that the mesh is a regular function of a vector of design parameters  $\beta$  (of size  $n_\beta$ ), then the implicit function theorem allows to define  $W$  as a function of  $X$  and so of  $\beta$  [48]. Discrete gradient calculation consists in computing the derivatives of  $n_f$  functions

$$\mathcal{J}_k(\beta) = J_k(W(\beta), X(\beta)), \quad 1 \leq k \leq n_f,$$

with respect to the  $n_\beta$  design parameters. In external aerodynamic applications,  $n_\beta$  is usually much larger than  $n_f$  and the most efficient way to proceed is to use the discrete adjoint method which requires to solve  $n_f$  linear systems

$$\left( \frac{\partial R}{\partial W} \right)^T \Lambda_k = - \left( \frac{\partial J_k}{\partial W} \right)^T, \quad 1 \leq k \leq n_f, \quad (10)$$

then to calculate

$$\frac{d \mathcal{J}_k}{d \beta} = \frac{\partial J_k}{\partial X} \frac{dX}{d \beta} + \Lambda_k^T \left( \frac{\partial R}{\partial X} \frac{dX}{d \beta} \right).$$

The dominant cost is the inversion of the  $n_f$  linear systems of size  $n_W$  whereas all other classical methods solve  $n_\beta$  linear (or possibly non-linear) systems of size  $n_W$ .

#### 3.2. Numerical characterization of discrete adjoint

The adjoint vector  $\Lambda$  associated to one function  $J$  is usually identified to the sensitivity of  $J$  to a perturbation of the residual  $R$  followed by re-convergence (see [12] and references therein). Following [1], we consider here a perturbation  $\delta R$  added in the right-hand-side of the discrete flow equations and denote by  $W + \delta W$  the converged solution corresponding to the perturbed equation:

$$R(W + \delta W, X) = \delta R,$$

or at first order

$$-\delta R + \frac{\partial R}{\partial W} \delta W = 0.$$

Since

$$J(W + \delta W, X) \simeq J(W, X) + \frac{\partial J}{\partial W} \delta W,$$

the first order change in the function of interest  $J$  due to change in flow  $\delta W$  is

$$\delta J = \frac{\partial J}{\partial W} \left( \frac{\partial R}{\partial W} \right)^{-1} \delta R.$$

Involving the discrete adjoint vector  $\Lambda$ , yields

$$\delta J = -\Lambda^T \delta R. \quad (11)$$

If only the  $a$ -th component of  $R$  at cell  $m$  has been arbitrarily altered by a small number  $\delta R_m^a$ , then (11) yields

$$\Lambda_m^a = -\delta J / \delta R_m^a, \quad (12)$$

which defines the  $a$ -th component of  $\Lambda$  at cell  $m$  as the limit ratio of the change in  $J$  divided by the infinitesimal change in the residual  $R$  at the corresponding cell and component which caused the change in flow and function value.

### 3.3. Physical characterization for 2D Euler flows

We here recall the physical interpretation of the adjoint solution by Giles and Pierce [1]. More precisely, the discussion in reference [1] is based on the continuous adjoint equation and its discrete counterpart is presented here. Four physical source terms  $\delta R$  are defined at each individual cell: 1) local mass source at fixed stagnation pressure and total enthalpy; 2) local normal force; 3) local change in total enthalpy at fixed static and total pressure; 4) local change in total pressure at fixed total enthalpy and static pressure:

$$\delta R_m^1 = \varepsilon \begin{pmatrix} 1 \\ u_x \\ u_y \\ H \end{pmatrix}, \quad \delta R_m^2 = \varepsilon \begin{pmatrix} 0 \\ -\rho u_y \\ \rho u_x \\ 0 \end{pmatrix}, \quad \delta R_m^3 = \varepsilon \begin{pmatrix} -\frac{1}{2H} \\ 0 \\ 0 \\ \frac{1}{2} \end{pmatrix}, \quad \delta R_m^4 = \varepsilon \begin{pmatrix} \left(\frac{\gamma-1}{\gamma} + \frac{1}{\gamma M^2}\right) \\ u_x \left(\frac{\gamma-1}{\gamma} + \frac{2}{\gamma M^2}\right) \\ u_y \left(\frac{\gamma-1}{\gamma} + \frac{2}{\gamma M^2}\right) \\ H \left(\frac{\gamma-1}{\gamma} + \frac{1}{\gamma M^2}\right) \end{pmatrix}, \quad 0 < \varepsilon \ll 1, \quad (13)$$

where  $p_0$ ,  $H$  and  $M$  denote the stagnation pressure, total enthalpy and Mach number, respectively.

At first order, the corresponding functions variations  $\delta J_m^1, \delta J_m^2, \delta J_m^3, \delta J_m^4$  due to the source terms in cell  $m$ , (13), read

$$(\delta J_m^1, \delta J_m^2, \delta J_m^3, \delta J_m^4) = -(\Lambda_m^1, \Lambda_m^2, \Lambda_m^3, \Lambda_m^4) \times \begin{pmatrix} \delta R_{1,m}^1 & \delta R_{1,m}^2 & \delta R_{1,m}^3 & \delta R_{1,m}^4 \\ \delta R_{2,m}^1 & \delta R_{2,m}^2 & \delta R_{2,m}^3 & \delta R_{2,m}^4 \\ \delta R_{3,m}^1 & \delta R_{3,m}^2 & \delta R_{3,m}^3 & \delta R_{3,m}^4 \\ \delta R_{4,m}^1 & \delta R_{4,m}^2 & \delta R_{4,m}^3 & \delta R_{4,m}^4 \end{pmatrix}, \quad (14)$$

where  $\delta J_m^d$  corresponds to the change in  $J$  due to  $d$ -th change of  $R$  in cell  $m$ . Reconverging flow  $W$  with a global change  $\delta W^d$  leads to the change  $\delta J_m^d$  of the function of interest. As the four changes in  $R$  are linearly independent, Giles and Pierce define the adjoint vector at cell  $m$  as the solution to (14) so, using the expression of the perturbation terms (13), we obtain

$$(\Lambda_m^1, \Lambda_m^2, \Lambda_m^3, \Lambda_m^4) = -(\delta J_m^1, \delta J_m^2, \delta J_m^3, \delta J_m^4) \times \frac{1}{\varepsilon} \begin{pmatrix} -1 - \frac{(\gamma-1)}{2} M^2 & -\frac{(1+(\gamma-1)M^2)u_x}{\|\bar{U}\|^2} & -\frac{(1+(\gamma-1)M^2)u_y}{\|\bar{U}\|^2} & \frac{1 + \frac{(\gamma-1)}{2} M^2}{H} \\ 0 & -\frac{u_y}{\rho \|\bar{U}\|^2} & \frac{u_x}{\rho \|\bar{U}\|^2} & 0 \\ -H & 0 & 0 & 1 \\ -\frac{\gamma M^2}{2} & \frac{\gamma u_x}{c^2} & \frac{\gamma u_y}{c^2} & -\frac{\gamma M^2}{2H} \end{pmatrix}. \quad (15)$$

The residual perturbation  $\delta R$  has thus been physically defined which makes the local discrete adjoint vector physically defined. For all systems of equations for which a similar demonstration can be done, the adjoint vector gets intrinsic and we can expect similar solutions from different discretizations and also mesh convergence. Let us finally note that not only the  $\Lambda$  components is of physical significance, but also the  $(\Lambda \cdot \delta R^d)/\varepsilon$  terms.

Finally, Giles and Pierce [1] have noted for continuous adjoint that the third perturbation does not alter the pressure field for inviscid flows and hence lets the drag and lift unchanged. From the expression of this perturbation, it is then straightforward to prove that lift and drag continuous adjoint fields satisfy all over the fluid domain the following equation:

$$\psi_1 = H\psi_4. \quad (16)$$

This property may be compared to (5) and is seen to be well satisfied in the numerical adjoint fields (see § 6.2.2). The fourth perturbation  $\delta R^4$  also preserves the static pressure at the source term location but the authors of reference [1] prove that, contrary to  $\delta R^3$ , for arbitrary flow conditions, it does preserve neither the static pressure field nor the streamtube structure of the base flows (in particular, the mass flux varies downwind the source term in the corresponding streamtube of the original flow).

#### 4. Adjoint-consistency of the cell-centered JST scheme

The question of dual consistency of the 2D cell-centered FV JST scheme is here analyzed by using the classical method of equivalent differential equation which consists in introducing Taylor series developments for all adjoint values to analyze the truncation error of the scheme [49, ch. 9]. We stress that this approach remains valid in the case of discontinuous solutions [50]. This analysis will be completed in § 6.1 to § 6.3 by the examination of the residuals of the continuous adjoint equation calculated for the discrete adjoint field. In the following we assume that the JST scheme is differentiable w.r.t. the degrees of freedom of the discrete direct problem which is a necessary condition for adjoint consistency. Situations of non-differentiability are discussed at the end of § 4.1.

Lozano studied the adjoint consistency of the discrete adjoint of the JST scheme for both cell-centered and cell-vertex discretizations [29] of the quasi-one-dimensional compressible Euler equations. Boundary conditions using artificial dissipation are applied which lead to inconsistent discrete adjoint scheme at the boundaries. Such boundary conditions are also not suitable for the simulation of internal flows that require conservativity. In this work we circumvent these difficulties by removing the dissipation at the boundary faces, while we modify the linearization at the penultimate cell to wall boundaries.

Jameson presented the continuous adjoint equations of 2D and 3D Euler equations in transformed coordinates [4]. Later on, Giles and Pierce derived the corresponding direct differentiation equation in 2D [51]. In this framework, the physical space (typically about an airfoil) is seen as the image of the unit domain  $[0, 1] \times [0, 1]$  with coordinates  $(\xi, \eta)$ . The transformed 2D Euler equations in the  $(\xi, \eta)$ -coordinates are well-known and, for functions of the form (1), the adjoint equations read

$$-\frac{\partial \Lambda^T}{\partial \xi} \left( \frac{\partial y}{\partial \eta} A(w) - \frac{\partial x}{\partial \eta} B(w) \right) - \frac{\partial \Lambda^T}{\partial \eta} \left( -A(w) \frac{\partial y}{\partial \xi} + B(w) \frac{\partial x}{\partial \xi} \right) = 0, \quad (17)$$

$A(w)$  and  $B(w)$  being the Jacobians of Euler flux in the physical  $x$  and  $y$  directions. The wall being defined by the  $\xi = 0$  boundary, if the function of interest is the force applied by the fluid on the solid in direction  $\vec{d} = (d_x, d_y)$ , then the corresponding boundary condition

$$-\Lambda^T \left( A(w) \frac{\partial y}{\partial \eta} - B(w) \frac{\partial x}{\partial \eta} \right) - \left( \frac{\partial y}{\partial \eta} d_x - \frac{\partial x}{\partial \eta} d_y \right) \frac{\partial p}{\partial W} = 0 \quad \text{at } \xi = 0$$

that can be simplified taking benefit of the specific form of the Jacobian at a wall yielding

$$\Lambda_2 \frac{\partial y}{\partial \eta} - \Lambda_3 \frac{\partial x}{\partial \eta} + \left( \frac{\partial y}{\partial \eta} d_x - \frac{\partial x}{\partial \eta} d_y \right) = 0. \quad (18)$$

The adjoint consistency of the FV scheme of interest is discussed hereafter referring to the analytic equations (17) and (18).

Using a structured mesh, the JST scheme in the  $i$ -direction reads (the  $j$  subscripts have been dropped for the sake of readability):

$$F_{i+1/2}^{JST} = \frac{1}{2} (\mathbf{F}(W_i) + \mathbf{F}(W_{i+1})) \cdot S_{i+1/2} - k^2 v_{i+1/2} \kappa_{i+1/2} (W_{i+1} - W_i) + \bar{k}_{i+1/2}^4 \kappa_{i+1/2} (W_{i+2} - 3W_{i+1} + 3W_i - W_{i-1}) \quad (19)$$

$$v_i = \frac{|p_{i+1} - 2p_i + p_{i-1}|}{(p_{i+1} + 2p_i + p_{i-1})} \quad v_{i+1/2} = \max(v_i, v_{i+1}) \quad (20)$$

$$\bar{k}_{i+1/2}^4 = \max(0, k^4 - v_{i+1/2} k^2) \quad \kappa_{i+1/2} = |\bar{U}_{i+1/2} \cdot S_{i+1/2}| + c_{i+1/2} \|S_{i+1/2}\|, \quad (21)$$

the fluid velocity and sound velocity at interface  $i + 1/2$  being derived from one of the classical conserved-variable means. Dual consistency close to the boundaries depends on the specific formulas applied at the border and close to border interfaces:

$$F_{3/2}^{JST} = \frac{1}{2} (\mathbf{F}(W_1) + \mathbf{F}(W_2)) \cdot S_{3/2} - k^2 v_{3/2} \kappa_{3/2} (W_2 - W_1) + \bar{k}_{3/2}^4 \kappa_{3/2} (W_3 - 3W_2 + 2W_1) \quad (22)$$

$$F_{1/2}^{JST} = \mathbf{F}(W_b) \cdot S_{1/2} \quad (23)$$

where  $p_0 = 2p_b - p_1$  is used in the evaluation of  $v_1$ , and  $W_b$  is a boundary state satisfying all Dirichlet-like boundary conditions.

Of course, at specific faces where either  $\bar{U} \cdot S = 0$ , or  $k^4 - vk^2 = 0$ , or  $v_i = v_{i+1}$ , the flux is not differentiable. This issue is discussed in [52] for a simulation about a symmetric airfoil, with a symmetric mesh and zero angle of attack leading to two complete lines of faces where  $|\bar{U} \cdot S|$  is extremely close to machine zero. The small irregularities of adjoint quantities that appear close to these lines are cured by regularization but no such problem is observed for more complex cases and, most generally, this question is discarded [53] considering that the occurrence of such equalities is marginal in practice.

Finally, we assume that the increments  $\Delta\xi$  and  $\Delta\eta$  between successive mesh points, have the same order of magnitude.

#### 4.1. Consistency of discrete adjoint inside the domain

Due to the four-point single-directional stencil, the discrete adjoint equation at a current cell  $(i, j)$  of the structured mesh reads

$$(\Lambda_{(i-2,j)}^T - \Lambda_{(i-1,j)}^T) \frac{\partial F_{i-3/2,j}}{\partial W_{(i,j)}} + (\Lambda_{(i-1,j)}^T - \Lambda_{(i,j)}^T) \frac{\partial F_{i-1/2,j}}{\partial W_{(i,j)}} \quad (24)$$

$$+ (\Lambda_{(i,j)}^T - \Lambda_{(i+1,j)}^T) \frac{\partial F_{i+1/2,j}}{\partial W_{(i,j)}} + (\Lambda_{(i+1,j)}^T - \Lambda_{(i+2,j)}^T) \frac{\partial F_{i+3/2,j}}{\partial W_{(i,j)}} \quad (25)$$

$$+ (\Lambda_{(i,j-2)}^T - \Lambda_{(i,j-1)}^T) \frac{\partial F_{i,j-3/2}}{\partial W_{(i,j)}} + (\Lambda_{(i,j-1)}^T - \Lambda_{(i,j)}^T) \frac{\partial F_{i,j-1/2}}{\partial W_{(i,j)}} \quad (26)$$

$$+ (\Lambda_{(i,j)}^T - \Lambda_{(i,j+1)}^T) \frac{\partial F_{i,j+1/2}}{\partial W_{(i,j)}} + (\Lambda_{(i,j+1)}^T - \Lambda_{(i,j+2)}^T) \frac{\partial F_{i,j+3/2}}{\partial W_{(i,j)}} = 0. \quad (27)$$

Only fluxes in the  $i$ -direction appear in lines (24)-(25), while only fluxes in the  $j$ -direction appear in lines (26)-(27). It is possible to analyze separately the two groups of corresponding terms. This is done below in the  $i$ -direction (again dropping the  $j$  subscripts). The contribution of the centered flux in the derivation of (24)-(25) is

$$\frac{1}{2} \left( (\Lambda_{i-1}^T - \Lambda_i^T) \frac{\partial \mathbf{F}}{\partial W_i} S_{i-1/2} + (\Lambda_i^T - \Lambda_{i+1}^T) \frac{\partial \mathbf{F}}{\partial W_i} S_{i+1/2} \right). \quad (28)$$

The  $i$  and  $j$  subscripts and  $\xi$  and  $\eta$  coordinates are linked by simple affine transformations

$$\xi(i) = \frac{i-1}{i_{max}-1} = (i-1)\Delta\xi \quad \eta(j) = \frac{j-1}{j_{max}-1} = (j-1)\Delta\eta$$

and the expression of the surface vectors is easily derived from those of the coordinates

$$S_{i+1/2,j} = \begin{pmatrix} y(\xi(i+1/2), \eta(j+1/2)) - y(\xi(i+1/2), \eta(j-1/2)) \\ -x(\xi(i+1/2), \eta(j+1/2)) + x(\xi(i+1/2), \eta(j-1/2)) \end{pmatrix}.$$

The two terms in (28) are hence consistent with

$$-\frac{1}{2} \frac{\partial \Lambda^T}{\partial \xi} \left( \frac{\partial y}{\partial \eta} A - \frac{\partial x}{\partial \eta} B \right) \Delta\xi \Delta\eta$$

respectively at points  $(i-1/2, j)$  and  $(i+1/2, j)$ , with  $\Delta\xi \Delta\eta$  denoting the volume of a cell, and the sum of both contributions is a consistent approximation of

$$-\frac{\partial \Lambda^T}{\partial \xi} \left( \frac{\partial y}{\partial \eta} A - \frac{\partial x}{\partial \xi} B \right) \Delta\xi \Delta\eta$$

at point  $(i, j)$ . Moreover it is second order accurate as it uses symmetric means and differences w.r.t.  $(\xi(i), \eta(j))$ . Carrying out the corresponding expansions for the linearized fluxes in  $j$ -direction, the second term of equation (17)



times  $\Delta\xi\Delta\eta$  is recovered. The first part of the discrete adjoint equation, obtained by isolating the derivation of the centered flux, is hence a consistent discretization of equation (17) up to a multiplicative  $\Delta\xi\Delta\eta$  factor.

After this first step, the discussion of the interior-cell adjoint consistency of JST scheme comes back to the examination of all the other terms of the equation (24)-(27). and the question whether other second order terms in  $\Delta\xi$  and  $\Delta\eta$  appear (no consistency) or only higher order terms appear (consistency). The terms of (24)-(25) that involve the derivation of the sensor, read

$$\begin{aligned}
& k^2 \left( (\Lambda_{i-2}^T - \Lambda_{i-1}^T) \frac{\partial v_{i-3/2}}{\partial W_{(i,j)}} \kappa_{i-3/2} \left( -(W_{i-2} - W_{i-1}) - 1_{[\bar{k}^4_{i-3/2} > 0]} (W_i - 3W_{i-1} + 3W_{i-2} - W_{i-3}) \right) \right. \\
& \quad + (\Lambda_{i-1}^T - \Lambda_i^T) \frac{\partial v_{i-1/2}}{\partial W_{(i,j)}} \kappa_{i-1/2} \left( -(W_{i-1} - W_i) - 1_{[\bar{k}^4_{i-1/2} > 0]} (W_{i+1} - 3W_i + 3W_{i-1} - W_{i-2}) \right) \\
& \quad + (\Lambda_i^T - \Lambda_{i+1}^T) \frac{\partial v_{i+1/2}}{\partial W_{(i,j)}} \kappa_{i+1/2} \left( -(W_i - W_{i+1}) - 1_{[\bar{k}^4_{i+1/2} > 0]} (W_{i+2} - 3W_{i+1} + 3W_i - W_{i-1}) \right) \\
& \quad \left. + (\Lambda_{i+1}^T - \Lambda_{i+2}^T) \frac{\partial v_{i+3/2}}{\partial W_{(i,j)}} \kappa_{i+3/2} \left( -(W_{i+1} - W_{i+2}) - 1_{[\bar{k}^4_{i+3/2} > 0]} (W_{i+3} - 3W_{i+2} + 3W_{i+1} - W_i) \right) \right), \quad (29)
\end{aligned}$$

where  $1_{[\bar{k}^4_{i+1/2} > 0]}$  stands for 1 if  $\bar{k}^4_{i+1/2}$  is strictly positive and 0 if not. As the spectral radius  $\kappa$  is  $O(\Delta\eta)$ , all the terms in (29) are at least  $O(\Delta\xi^2\Delta\eta)$ . The terms of (24)-(25) that involve the derivation of the spectral radius are

$$\begin{aligned}
& (\Lambda_{i-1}^T - \Lambda_i^T) \frac{\partial \kappa_{i-1/2}}{\partial W_{(i,j)}} \left( -k^2 v_{i-1/2} (W_{i-1} - W_i) + \bar{k}^4_{i-1/2} (W_{i+1} - 3W_i + 3W_{i-1} - W_{i-2}) \right) \\
& (\Lambda_i^T - \Lambda_{i+1}^T) \frac{\partial \kappa_{i+1/2}}{\partial W_{(i,j)}} \left( -k^2 v_{i+1/2} (W_i - W_{i+1}) + \bar{k}^4_{i+1/2} (W_{i+1} - 3W_i + 3W_{i-1} - W_{i-2}) \right). \quad (30)
\end{aligned}$$

As  $\kappa_{i-1/2}$  and its derivatives w.r.t.  $W$  are  $O(\Delta\eta)$  and as  $v_{i-1/2}$  is  $O(\Delta\xi^2)$  these terms are  $O(\Delta\xi^4\Delta\eta)$ . The terms arising when deriving the first and third-order differences are

$$\begin{aligned}
& (\Lambda_{i-2}^T - \Lambda_{i-1}^T) (\kappa_{i-3/2} \bar{k}^4_{i-3/2}) + (\Lambda_{i-1}^T - \Lambda_i^T) (k^2 v_{i-1/2} \kappa_{i-1/2} - 3\bar{k}^4_{i+1/2} \kappa_{i-1/2}) \\
& + (\Lambda_i^T - \Lambda_{i+1}^T) (-k^2 v_{i+1/2} \kappa_{i+1/2} + 3\bar{k}^4_{i+1/2} \kappa_{i+1/2}) + (\Lambda_{i+1}^T - \Lambda_{i+2}^T) (-\kappa_{i+3/2} \bar{k}^4_{i+3/2}),
\end{aligned}$$

and may be rewritten as

$$\begin{aligned}
& (\Lambda_{i-2}^T - \Lambda_{i-1}^T) \kappa_{i-3/2} \bar{k}^4_{i-3/2} - 3(\Lambda_{i-1}^T - \Lambda_i^T) \kappa_{i-1/2} \bar{k}^4_{i-1/2} \\
& + 3(\Lambda_i^T - \Lambda_{i+1}^T) \kappa_{i+1/2} \bar{k}^4_{i+1/2} - (\Lambda_{i+1}^T - \Lambda_{i+2}^T) \kappa_{i+3/2} \bar{k}^4_{i+3/2} \\
& - k^2 ((\Lambda_{i-1}^T - \Lambda_i^T) v_{i-1/2} \kappa_{i-1/2} - (\Lambda_i^T - \Lambda_{i+1}^T) v_{i+1/2} \kappa_{i+1/2}).
\end{aligned}$$

The last two terms that stem from first-difference dissipation fluxes, are both  $O(\Delta\xi^3\Delta\eta)$  as the sensor in  $\xi$  ( $I$ -mesh) direction is  $O(\Delta\xi^2)$ . The possibly problematic terms are the four first terms stemming from the third-difference dissipation fluxes. These are individually  $O(\Delta\xi\Delta\eta)$  terms and the question is whether their linear combination is a higher order term. If the algebraic expression of  $\bar{k}^4$  as function of the state variables is the same for all four values, then a third order difference is identified and linear combination of these four terms is  $O(\Delta\xi^4\Delta\eta)$ . If some of the  $v_{i+1/2}$  are equal to the left value  $v_i$  and some to the right value  $v_{i+1}$  but none of the  $\bar{k}_4$  is zero, the terms stemming from the derivation of third-order differences may be rewritten

$$\begin{aligned}
& (\Lambda_{i-2}^T - \Lambda_{i-1}^T) \kappa_{i-3/2} k^4 - 3(\Lambda_{i-1}^T - \Lambda_i^T) \kappa_{i-1/2} k^4 + 3(\Lambda_i^T - \Lambda_{i+1}^T) \kappa_{i+1/2} k^4 - (\Lambda_{i+1}^T - \Lambda_{i+2}^T) \kappa_{i+3/2} k^4 \\
& - (\Lambda_{i-2}^T - \Lambda_{i-1}^T) \kappa_{i-3/2} k^2 v_{i-3/2} + 3(\Lambda_{i-1}^T - \Lambda_i^T) \kappa_{i-1/2} k^2 v_{i-1/2} \\
& - 3(\Lambda_i^T - \Lambda_{i+1}^T) \kappa_{i+1/2} k^2 v_{i+1/2} + (\Lambda_{i+1}^T - \Lambda_{i+2}^T) \kappa_{i+3/2} k^2 v_{i+3/2}.
\end{aligned}$$

In this case, the sum of the terms involving  $k^4$  is  $O(\Delta\xi^4\Delta\eta)$  and the terms in  $k_2$  may be individually identified as  $O(\Delta\xi^3\Delta\eta)$  terms. For inconsistency to be observed, it is hence necessary that: (a) due to the max in equation (20), the actual formulas of the involved  $\bar{k}^4$  are not the same up to a shift of subscripts; (b) some of the  $\bar{k}^4$  are zero. (Note that these conditions are expected to appear at a marginal number of cells in particular as  $v$  is very close to zero except in the vicinity of shockwaves. Also note that these conditions are not event sufficient for dual inconsistency – if  $\bar{k}^4_{i-3/2} = \bar{k}^4_{i+3/2} = 0$  and  $k^4_{i+1/2} \neq 0$ ,  $\bar{k}^4_{i+3/2} \neq 0$  or crisscross, dual-consistency is observed). Such conditions for inconsistency thus correspond to local non-differentiability of the JST scheme and may be compared with the results of reference [30] and the local lack of dual consistency of the studied schemes where upwinding changes.

#### 4.2. Consistency of the discrete adjoint at a penultimate cell w.r.t. a boundary

In a penultimate cell of subscript  $(2, j)$ , the previous equations are slightly altered as fluxes  $F_{1/2, j}$  and  $F_{3/2, j}$  have specific definitions involving a boundary state,  $W_{b_{1/2, j}}$ . Actually  $W_{b_{1/2, j}}$  is derived only from the adjacent conservative variables  $W_{1, j}$  for each boundary interface;  $W_b$  satisfies all Dirichlet like relations to be imposed at the boundary. The numerical fluxes at interfaces  $3/2$  and  $1/2$  are given in (22) and (23), respectively.

As concerning the discrete adjoint equation of penultimate cell  $(2, j)$  (see Fig. 1), note first that the contributions of the centered flux are standard for both mesh direction since  $F_{1/2, j}^{JST}$  does not depend on  $W_{2, j}$ . The terms of lines (26)-(27) are the same as in a current cell and do not need to be investigated again. The examination of those of lines (24)-(25) is done first considering the derivation of the sensor and the spectral radius. As the resulting contributions to the discrete adjoint equation have been bounded individually in the previous subsection, it is only needed to look at the specific contributions of faces  $(1/2, j)$  and  $(3/2, j)$ . No artificial dissipation is introduced at  $(1/2, j)$ , while deriving the sensors in  $F_{3/2}^{JST}$  yields

$$(\Lambda_1^T - \Lambda_2^T) \frac{\partial v_{3/2}}{\partial W_2} \kappa_{3/2} \left( - (W_1 - W_2) - 1_{[\bar{k}^4_{3/2} > 0]} (W_3 - 3W_2 + 2W_1) \right)$$

which is  $O(\Delta\xi^2\Delta\eta)$ . The corresponding terms for  $F_{5/2}^{JST}$  and  $F_{7/2}^{JST}$  are at least  $O(\Delta\xi^2\Delta\eta)$  as justified in the previous subsection. When deriving the spectral radius, the only specific term, depending on the boundary condition, is the one stemming from  $F_{3/2}^{JST}$ ,

$$(\Lambda_1^T - \Lambda_2^T) \frac{\partial \kappa_{3/2}}{\partial W_2} \left( -k^2 v_{3/2} (W_1 - W_2) + \bar{k}^4_{3/2} (W_3 - 3W_2 + 2W_1) \right).$$

The first part of this expression is  $O(\Delta\xi^3\Delta\eta)$  (a more precise assertion depends whether  $v_{3/2} = v_1$  (that is  $O(\Delta\xi)$ ) or  $v_{3/2} = v_2$  that is  $O(\Delta\xi^2)$ ). The second part of this expression is  $O(\Delta\xi^2\Delta\eta)$ . None of them hence prevents dual consistency. Finally, the terms arising from the derivation of the differences terms in (24)-(25) read

$$(\Lambda_1^T - \Lambda_2^T) (-k^2 v_{3/2} \kappa_{3/2} - 3\bar{k}^4_{3/2} \kappa_{3/2}) + (\Lambda_2^T - \Lambda_3^T) (k^2 v_{5/2} \kappa_{5/2} + 3\bar{k}^4_{5/2} \kappa_{5/2}) + (\Lambda_3^T - \Lambda_4^T) (-\kappa_{7/2} \bar{k}^4_{7/2}).$$

They may be rewritten as

$$\begin{aligned} & -3(\Lambda_1^T - \Lambda_2^T) \bar{k}^4_{3/2} \kappa_{3/2} + 3(\Lambda_2^T - \Lambda_3^T) \bar{k}^4_{5/2} \kappa_{5/2} - (\Lambda_3^T - \Lambda_4^T) \kappa_{7/2} \bar{k}^4_{7/2} \\ & - (\Lambda_1^T - \Lambda_2^T) k^2 v_{3/2} \kappa_{3/2} + (\Lambda_2^T - \Lambda_3^T) k^2 v_{5/2} \kappa_{5/2}. \end{aligned}$$

The two-term difference of the last line is  $O(\Delta\xi^4\Delta\eta)$ . The sum of the terms of the first line is only  $O(\Delta\xi\Delta\eta)$  and introduces an inconsistency. Compared to the current-point equation, due to the specific  $F_{1/2, j}$  formula, a  $(\Lambda_0^T - \Lambda_1^T) \bar{k}^4_{1/2} \kappa_{1/2}$  is missing to have a third-difference appear.

How the scheme can be corrected and the discrete adjoint can be slightly modified to obtain dual-consistency is discussed in § 4.4.

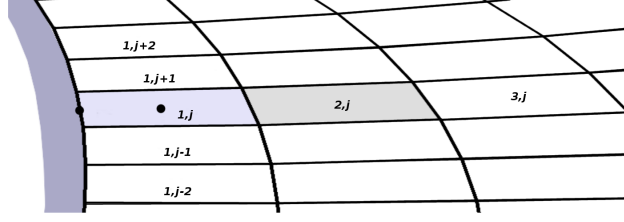


Figure 1: Location of the state variable  $W$  and the corresponding boundary variable  $W_b$  for the  $(1, j)$  cell. Stencil of the JST scheme for this cell.

#### 4.3. Consistency of discrete adjoint at a wall boundary cell

Considering an output of the form (1) that depends on the wall boundary variable,  $W_b$ , the discrete adjoint equation in a cell adjacent to a wall-boundary reads (see cell  $(1, j)$  in Fig. 1)

$$\sum_k \Lambda_k^T \frac{\partial R_k}{\partial W_{(1,j)}} = - \frac{\partial J}{\partial W_{b(1/2,j)}} \frac{\partial W_{b(1/2,j)}}{\partial W_{(1,j)}}. \quad (31)$$

Due to the stencil of JST scheme in (19), (22) and (23), the  $k$  subscript varies in  $\{(1, j-2), (1, j-1), (1, j), (1, j+1), (1, j+2), (2, j), (3, j)\}$  (see Fig. 1). The expanded expression of (31) reads

$$(\Lambda_{(1,j-2)}^T - \Lambda_{(1,j-1)}^T) \frac{\partial F_{1,j-3/2}}{\partial W_{(1,j)}} + (\Lambda_{(1,j-1)}^T - \Lambda_{(1,j)}^T) \frac{\partial F_{1,j-1/2}}{\partial W_{(1,j)}} \quad (32)$$

$$+ (\Lambda_{(1,j)}^T - \Lambda_{(1,j+1)}^T) \frac{\partial F_{1,j+1/2}}{\partial W_{(1,j)}} + (\Lambda_{(1,j+1)}^T - \Lambda_{(1,j+2)}^T) \frac{\partial F_{1,j+3/2}}{\partial W_{(1,j)}} \quad (33)$$

$$+ (\Lambda_{(2,j)}^T - \Lambda_{(3,j)}^T) \frac{\partial F_{5/2,j}}{\partial W_{(1,j)}} + (\Lambda_{(1,j)}^T - \Lambda_{(2,j)}^T) \frac{\partial F_{3/2,j}}{\partial W_{(1,j)}} \quad (34)$$

$$- \Lambda_{(1,j)}^T \frac{\partial F_{1/2,j}}{\partial W_{(j,1)}} = - \frac{\partial J}{\partial W_{b(i,1/2)}} \frac{\partial W_{b(i,1/2)}}{\partial W_{(1,j)}}. \quad (35)$$

It is clear that the terms of line (35) are  $O(\Delta\eta)$ . The  $J$  derivative fluxes appearing in (32) (33) are standard fluxes in the  $i$ -direction of the form (19) that do not depend on the boundary condition. The maximum order of magnitude of the various terms of these lines is hence  $O(\Delta\xi\Delta\eta)$  (obtained when differentiating the centered flux). Whatever the specific complexity of the  $(\partial F_{i,3/2}/\partial W_{(1,j)})$  terms due to the boundary state  $W_b(W_{(1,j)})$ , all terms appearing in line (34) are at least  $O(\Delta\xi\Delta\eta)$ . Keeping only the  $O(\Delta\eta)$  terms, previous equations yields

$$- \Lambda_{(i,1)}^T \begin{pmatrix} 0 \\ Sx_{(1/2,j)} \\ Sy_{(1/2,j)} \\ 0 \end{pmatrix} \frac{\partial p_{b(1/2,j)}}{\partial W_{b(1/2,j)}} \frac{\partial W_{b(1/2,j)}}{\partial W_{(1,j)}} \simeq - \frac{\partial((-S_{(1/2,j)} \cdot \bar{d}) p_{b(1/2,j)})}{\partial W_{b(1/2,j)}} \frac{\partial W_{b(1/2,j)}}{\partial W_{(1,j)}}.$$

That is simplified in

$$\Lambda_{(i,1)}^2 Sx_{(1/2,j)} + \Lambda_{(i,1)}^3 Sy_{(1/2,j)} \simeq -\overline{S_{(1/2,j)}} \cdot \bar{d}. \quad (36)$$

Equation (36) is obviously the cell-centered FV counterpart of the continuous adjoint wall boundary condition (8) in the Cartesian frame. Note that it involves metric terms at the wall and the adjoint solution at adjacent cells and also that it has been derived by equalizing lower-order (i.e., first-order) terms in space. How accurately equation (36) is satisfied is discussed in sections 6.1 to 6.3.

#### 4.4. Modified discrete adjoint for adjoint consistency

The discrete adjoint of the cell-centered JST scheme (19), (22) and (23) is thus adjoint-consistent except at penultimate cells w.r.t. a boundary. This issue is considered here. A satisfactory modification of  $F_{3/2}^{JST}$  for dual consistency, would be

$$F_{3/2} = \frac{1}{2}(\mathbf{F}(W_1) + \mathbf{F}(W_2)) \cdot S_{3/2} - k^2 v_{3/2} \kappa_{3/2} (W_2 - W_1) + \bar{k}^4_{3/2} \kappa_{3/2} (W_3 - 2W_2 + W_1)$$

Unfortunately, as there is no artificial dissipation in  $F_{1/2}$  so that the  $\bar{k}^4_{3/2} \kappa_{3/2} (W_3 - 2W_2 + W_1)$  term of this modified  $F_{3/2}$  would introduce an anti-dissipative term in the equivalent equation of the cell adjacent to the boundary that may result in a significant loss of robustness. This variant has hence not been considered.

Adjoint-consistency can otherwise be recovered at the price of a minor and local approximation in the Jacobian of the scheme. Following the calculations of § 4.2, the needed change in the differentiation of the  $F_{3/2,j}$  flux is the replacement of

$$-3(\Lambda_1^T - \Lambda_2^T) \bar{k}^4_{3/2} \kappa_{3/2} \quad \text{by} \quad -2(\Lambda_1^T - \Lambda_2^T) \bar{k}^4_{3/2} \kappa_{3/2} \quad \text{in} \quad (\partial F_{3/2,j} / \partial W_2)$$

when differentiating the third order difference. Although all adjoint values are coupled, this induces no significant change far from the boundaries. Close to the wall, this change makes the contours more regular and lowers the maximum values of the adjoint field as observed in Fig. 2 for a transonic flow about the NACA0012. Besides it is noted that adjoint contours are stretched close de penultimate cells w.r.t. the boundary for the inconsistent exact discrete adjoint (Fig. 2 left). Moreover, when plotting the residual of the continuous adjoint equation discretized on the mesh with the computed flow and discrete discrete adjoint (see Fig. 3 for the same transonic flow), lower values are observed for the consistent adjoint variant.

Due to these observations, the slightly modified and dual-consistent discrete adjoint is used when discussing mesh convergence and asymptotic behavior at the stagnation streamline and at the wall. In all other sections, the exact discrete adjoint solution of the scheme is retained.

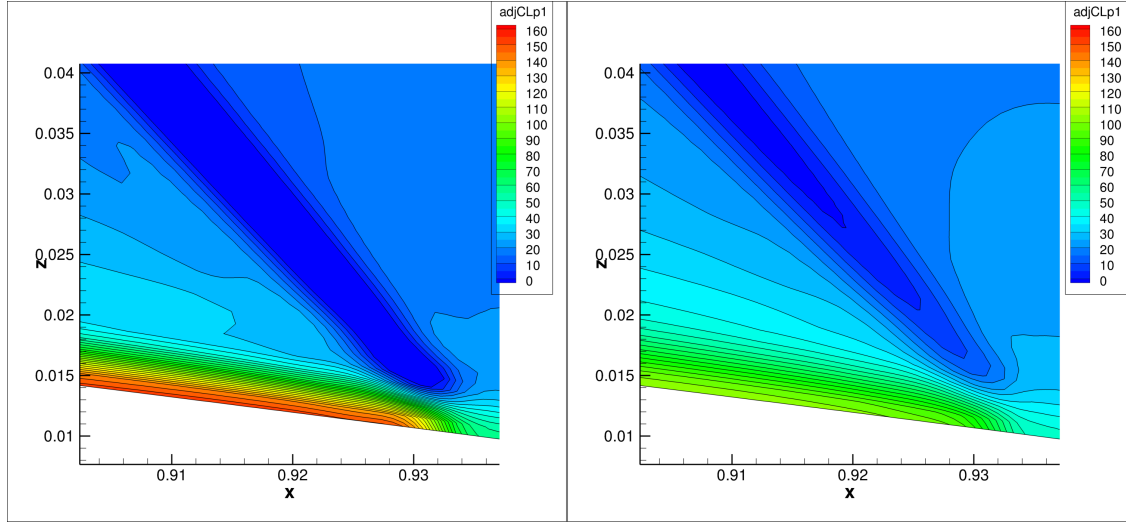


Figure 2: ( $M_\infty = .85$ ,  $\alpha = 2^\circ$ ,  $2049 \times 2049$  mesh) First component of  $\Lambda_{CL_p}$ : inconsistent discrete adjoint (left) and consistent discrete adjoint (right).

## 5. Adjoint Rankine-Hugoniot relations

We consider an isolated discontinuity  $\Sigma$  where the direct solution satisfies the RH jump relations

$$[[n_x F_x(W) + n_y F_y(W)]] = 0, \tag{37}$$

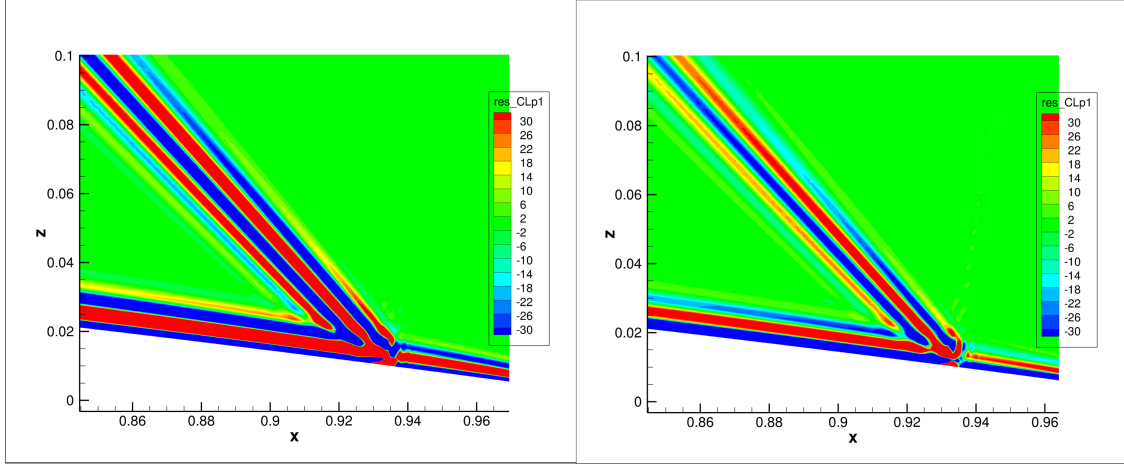


Figure 3: ( $M_\infty = 0.85$ ,  $\alpha = 2^\circ$ ,  $2049 \times 2049$  mesh) First component of lift continuous adjoint equation discretized on the mesh with inconsistent discrete adjoint field (left) and consistent discrete adjoint field (right).

where  $[[\cdot]]$  denotes the jump across  $\Sigma$  and  $\bar{n} = (n_x, n_y)^T$  is the normal to  $\Sigma$ . Introducing  $\bar{t} = (-n_y, n_x)^T$ , the adjoint equation (4) may be rewritten as

$$-A_n^T \frac{\partial \psi}{\partial n} - A_t^T \frac{\partial \psi}{\partial t} = 0 \quad \text{in } \Omega, \quad (38)$$

with

$$A_n = n_x A + n_y B = \begin{pmatrix} 0 & n_x & n_y & 0 \\ (\gamma-1)e_c n_x - uv_n & v_n - (\gamma-2)un_x & un_y - (\gamma-1)vn_x & (\gamma-1)n_x \\ (\gamma-1)e_c n_y - vv_n & vn_x - (\gamma-1)un_y & v_n - (\gamma-2)vn_y & (\gamma-1)n_y \\ ((\gamma-1)e_c - H)v_n & Hn_x - (\gamma-1)uv_n & Hn_y - (\gamma-1)vv_n & \gamma v_n \end{pmatrix},$$

$$A_t = -n_y A + n_x B = \begin{pmatrix} 0 & -n_y & n_x & 0 \\ -(\gamma-1)e_c n_y - uv_t & v_t + (\gamma-2)un_y & un_x + (\gamma-1)vn_y & -(\gamma-1)n_y \\ (\gamma-1)e_c n_x - vv_t & -vn_y + (\gamma-1)un_x & v_t - (\gamma-2)vn_x & (\gamma-1)n_x \\ ((\gamma-1)e_c - H)v_t & -Hn_y - (\gamma-1)uv_t & Hn_x - (\gamma-1)vv_t & \gamma v_t \end{pmatrix},$$

where  $v_n = \bar{n} \cdot \bar{U}$ ,  $v_t = \bar{t} \cdot \bar{U}$ ,  $\partial_n \psi = n_x \partial_x \psi + n_y \partial_y \psi$ , and  $\partial_t \psi = -n_y \partial_x \psi + n_x \partial_y \psi$ . Assuming that  $A_n$  is non-singular, the adjoint is continuous across  $\Sigma$  [36, 1, 38, 37]:  $[[\psi]] = 0$ , so  $[[\partial_t \psi]] = 0$ . Likewise we have  $[[\rho v_n]] = 0$ ,  $[[v_t]] = 0$ , and  $[[H]] = 0$ .

Let (38a-d) denote the four equations in (38). Then, the manipulation  $(38a) + \frac{u_x}{2}(38b) + \frac{u_y}{2}(38c)$  gives

$$\frac{v_n}{2} (\partial_n \psi_1 - H \partial_n \psi_4) + \frac{v_t}{2} (\partial_t \psi_1 - H \partial_t \psi_4) = 0,$$

and applying the jump operator we obtain

$$[[v_n \partial_n \psi_1]] - H [[v_n \partial_n \psi_4]] = 0. \quad (39)$$

(For functions of the static pressure and the geometry, according to equation (16), we expect the left and right terms of the difference to be zero which is actually observed later on in the numerical experiments with lift and drag adjoint.)

Likewise, (38d) gives

$$(\gamma-1) [[n_x \partial_n \psi_2 + n_y \partial_n \psi_3]] + \gamma [[v_n \partial_n \psi_4]] = 0. \quad (40)$$

Now, the operations  $[[n_x(38c)-n_y(38b)]]$  and  $[[n_x(38b)+n_y(38c)]]$  provide

$$[[v_n(-n_y\partial_n\psi_2+n_x\partial_n\psi_3+v_t\partial_n\psi_4)]]+[[v_n]](n_x\partial_t\psi_2+n_y\partial_t\psi_3)=0, \quad (41a)$$

$$[[\partial_n\psi_1]]+[[u+v_n n_x]\partial_n\psi_2+(v+v_n n_y)\partial_n\psi_3+(H+v_n^2)\partial_n\psi_4]+[[v_n]]v_t\partial_t\psi_4=0. \quad (41b)$$

Finally, the adjoint equation to the RH relations (37) reads  $[-n_y F_x(W)+n_x F_y(W)] \cdot \partial_t \psi = 0$  [36, 38, 37] which may be simplified into

$$v_t [[\rho]] (\partial_t \psi_1 + H \partial_t \psi_4) + ([[p]] + v_t^2 [[\rho]]) (-n_y \partial_t \psi_2 + n_x \partial_t \psi_3) = 0. \quad (42)$$

## 6. Numerical experiments

We consider the direct and adjoint solutions for inviscid flows around the NACA0012 airfoil in different regimes. Steady-state solutions are computed on a series of five structured meshes (ranging from  $129 \times 129$  to  $4097 \times 4097$  nodes) used and described in [54] with the *elsA* code [55]. The farfield boundary is set at about 150 chords. The computations have been converged with a second order accurate finite volume method using the JST scheme (19), (22) and (23) with  $k^2 = 0.5$  and  $k^4 = 0.032$ , except for the subsonic flow for which we used  $k_2 = 0$  and  $k_4 = 0.032$ . The adjoint consistent linearization of the JST scheme is used for the computation of the adjoint fields (see § 4.4) associated to the drag and lift coefficients.

The derivatives of the lift and drag w.r.t. the flow field variables in the discrete adjoint equation (10) are calculated by using the post-processing tool from [56] before the adjoint equations are solved by the adjoint module of *elsA* [57] for the two functions and the complete set of meshes.

### 6.1. Supersonic regime

We first consider a supersonic flow about the NACA0012 airfoil with a free-stream Mach number of  $M_\infty = 1.5$  and an angle of attack  $\alpha = 1^\circ$ .

The solution is displayed in Fig. 4. The flow is supersonic and constant up to a detached shock wave. Downstream the shock wave, the flow is subsonic in a small bubble close to the airfoil leading edge and supersonic elsewhere. It accelerates along the airfoil up to a fishtail shock wave based on the trailing edge. Downstream this second shock wave, the flow is still supersonic with a Mach number close to the upwind farfield Mach number.

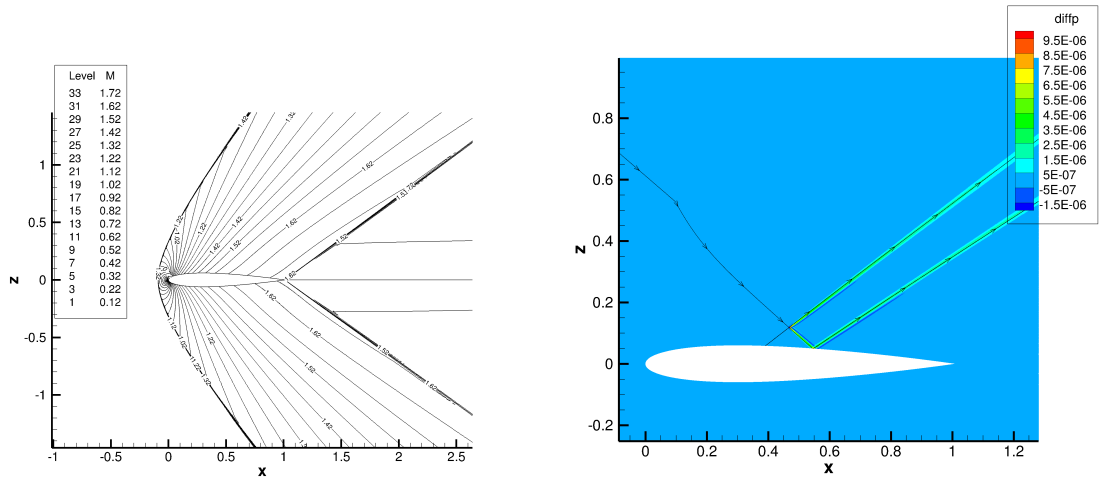


Figure 4: ( $M_\infty = 1.50$ ,  $\alpha = 1^\circ$ ,  $2049 \times 2049$  mesh) Left: contours of Mach number. Right: Change in pressure due to  $\delta R^1$  source term ( $\varepsilon=6.10^{-6}$ ) at point ( $x = 0.4702, y = 0.1184$ ).

### 6.1.1. Lift and drag adjoint solutions

Figure A.26 presents the contours of all four components of the adjoint fields.

The gradient of the discrete adjoint is then estimated at cell centers using Green formula and finally the residual in cell  $(i, j)$  of the continuous adjoint equation,

$$res_{ij} = -A_{ij}^T \left( \frac{\partial \Lambda}{\partial x} \right)_{ij} - B_{ij}^T \left( \frac{\partial \Lambda}{\partial y} \right)_{ij}, \quad (43)$$

is evaluated for both functions. In the above equation,  $A_{ij}$  and  $B_{ij}$  are the Jacobians evaluated with cell-center values. For a first verification, both terms of the residual and their sum are plotted separately for the lift, on the  $2049 \times 2049$  mesh in Fig. 5 and then added in Fig. 6 (top left). The cancellation of almost opposite terms is obvious. The percentage of cells with  $|res|$  below a threshold is decreasing as the mesh is refined. Nevertheless significant (and increasing)  $|res|$  values are still observed on the finest meshes at the trailing edge and along the Mach lines passing through the trailing edge (where a perfect adjoint field would exhibit a discontinuity due to the end of the function support) – see Fig. 6.

Concerning farfield boundary conditions, the normal Mach number appears to be supersonic at the intersection of the characteristic geometrical strips (see Fig. 7) and the far field boundary. No continuous adjoint boundary conditions is hence to be applied there and no check of discrete versus continuous adjoint is required. Concerning the discrete equation (36) that is the counterpart of the continuous boundary condition at the wall, equation (8), its two terms are plotted in the right part of Fig. 6. They appear to be superimposed so that (36) is actually well satisfied.

Besides, as a mean to check the mesh convergence of adjoint fields, we have calculated the finest mesh adjoint-lift and adjoint-drag on another  $2049 \times 2049$  mesh. The corresponding adjoint field in Fig. A.19 can almost not be distinguished from the one obtained with the nominal mesh. This is an illustration of the intrinsic nature of adjoint supported by Giles and Pierce analysis.

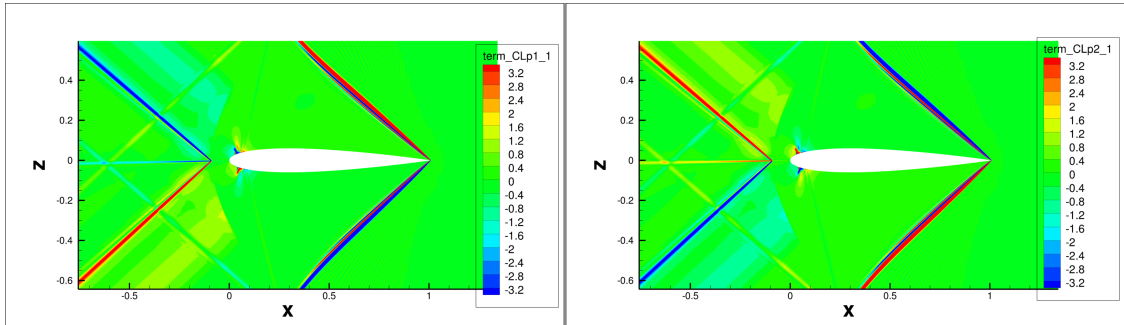


Figure 5: ( $M_\infty = 1.5$ ,  $\alpha = 1^\circ$ ,  $2049 \times 2049$  mesh) Left:  $-A^T (\partial \Lambda_{CLp1} / \partial x)$  discretized with discrete adjoint field (first component of the vector). Right:  $-B^T (\partial \Lambda_{CLp2} / \partial y)$  discretized with discrete adjoint field (idem).

### 6.1.2. Adjoint fields upstream of the shock

The flow is supersonic and constant upstream of the detached shock wave so that the Jacobians  $A$  and  $B$  in the continuous adjoint equation (4) are constant matrices in this area that enables a specific analysis of the continuous adjoint solution in this region. This analysis, partly presented in [42] is here further developed and assessed. In a supersonic regime, the direct and adjoint equations both exhibit specific directions of propagation corresponding to simple waves solutions to (4):

$$\psi(x, y) = \phi(x \sin(\gamma) - y \cos(\gamma)) \lambda_0,$$

where  $\gamma$  is the angle made by the direction of propagation with the x-axis,  $\lambda_0$  is a vector representing the convected information and  $\phi$  is a scalar function. Injecting this expression into (4) yields

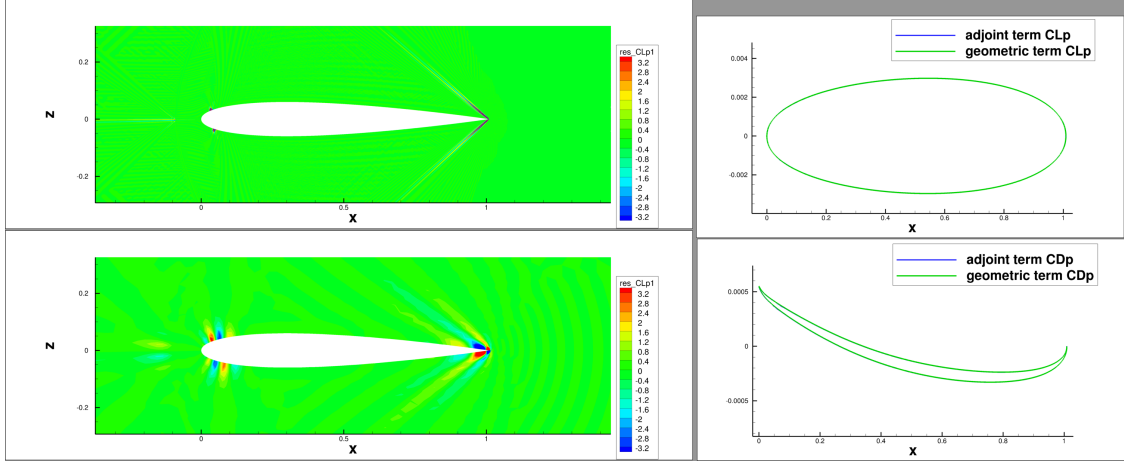


Figure 6: ( $M_\infty = 1.5$ ,  $\alpha = 1^\circ$ ) Left: Residual of the continuous equation (first component) evaluated with the lift discrete adjoint fields (bottom:  $129 \times 129$  mesh, top:  $2049 \times 2049$  mesh), right: geometric and adjoint terms of equation (36) for lift and drag ( $2049 \times 2049$  mesh)

$$\phi'(x \sin(\gamma) - y \cos(\gamma)) \times (\sin(\gamma)A^T - \cos(\gamma)B^T)\lambda_0 = 0.$$

This equation admits a non-trivial solution  $\lambda_0$  if and only if

$$\det(\sin(\gamma)A^T - \cos(\gamma)B^T) = 0.$$

This condition is the same as the for supersonic Euler equations since the transposition plays no role in the calculation of the determinant. The eigenvalues of  $\sin(\gamma)A - \cos(\gamma)B$  are:  $(u_x \sin(\gamma) - u_y \cos(\gamma), u_x \sin(\gamma) - u_y \cos(\gamma) + c, u_x \sin(\gamma) - u_y \cos(\gamma) - c)$ . Since one of the eigenvalues vanishes,  $\gamma$  is solution of one of these equations:

$$u_x \sin(\gamma) - u_y \cos(\gamma) = 0, \quad u_x \sin(\gamma) - u_y \cos(\gamma) + c = 0, \quad u_x \sin(\gamma) - u_y \cos(\gamma) - c = 0.$$

Let  $\alpha$  denote the angle of incidence, then the velocity components then read  $u_x = \|\bar{U}\| \cos(\alpha)$  and  $u_y = \|\bar{U}\| \sin(\alpha)$ . Substituting these expressions in the above relations yields

$$\begin{aligned} \gamma &= \alpha \quad \text{or} \quad \alpha + \pi \\ \gamma &= \alpha - \mu \quad \text{or} \quad \gamma = \alpha - \mu + \pi \\ \gamma &= \alpha + \mu \quad \text{or} \quad \gamma = \alpha + \mu + \pi, \end{aligned}$$

where  $\mu = \arcsin(1/M_\infty)$  is the Mach angle. Hence, the information propagates along the three privileged directions  $\gamma = \alpha$ ,  $\gamma = \alpha - \mu$  et  $\gamma = \alpha + \mu$ . Evidently, the domains of influence/dependance are inverse one another for state and adjoint variables.

The  $\lambda_0$  eigenvectors of interest are those of  $\sin(\gamma)A^T - \cos(\gamma)B^T$ . These are also the left eigenvectors that appear in the more classical diagonalization of the inviscid flux Jacobian. Following [49], the (left) eigenvector associated to  $\gamma = \alpha - \mu$  (null eigenvalue  $u_x \sin(\gamma) - u_y \cos(\gamma) + c$ ) and  $\gamma = \alpha + \mu$  (null eigenvalue  $u_x \sin(\gamma) - u_y \cos(\gamma) - c$ ) are

$$\lambda_0^{\alpha-\mu} = \begin{pmatrix} \frac{c}{\rho} \left( \frac{-u_x n_x - u_y n_y}{2c} + \frac{(\gamma-1)}{2} M^2 \right) \\ \frac{1}{\rho} \left( n_x c - (\gamma-1) \frac{u_x}{\rho} \right) \\ \frac{1}{\rho} \left( n_y c - (\gamma-1) \frac{u_y}{\rho} \right) \\ \frac{\gamma-1}{\rho c} \end{pmatrix}, \quad \lambda_0^{\alpha+\mu} = \begin{pmatrix} \frac{c}{\rho} \left( \frac{u_x n_x + u_y n_y}{2c} + \frac{(\gamma-1)}{2} M^2 \right) \\ \frac{1}{\rho} \left( n_x + (\gamma-1) \frac{u_x}{c} \right) \\ \frac{1}{\rho} \left( n_y + (\gamma-1) \frac{u_y}{c} \right) \\ \frac{\gamma-1}{\rho c} \end{pmatrix},$$



for a general direction  $(n_x, n_y)^T$ , which may be replaced by  $(\sin(\gamma), -\cos(\gamma))$  to recover the solution as a function of the simple wave angles. Checking that the simple waves solution satisfy relation (16) uses the nullity of the eigenvalue ( $u_x n_x + u_y n_y + c = 0$  for the first vector and  $u_x n_x + u_y n_y - c = 0$  for the second eigenvector).

The dimension of the eigenspace associated to  $\gamma = \alpha$  is two but the classically exhibited left eigenvectors [49] do not satisfy the Giles and Pierce relation for pressure-based outputs (16). The vectors of this 2D space that satisfy this relation is the 1D space generated by

$$\lambda_0^\alpha = \begin{pmatrix} -1 - \frac{(\gamma-1)q^2}{2c^2} \\ \frac{(\gamma-1)u_x}{c^2} + \frac{2n_y}{n_y u_x - n_x u_y} \\ \frac{(\gamma-1)u_y}{c^2} - \frac{2n_x}{n_y u_x - n_x u_y} \\ -\frac{\gamma-1}{\rho c} \end{pmatrix}$$

Figure 7 highlights the directions of propagation in the first component discrete adjoint field. The ratio of the adjoint components inside all three geometrical strips is found equal to the ratio of the corresponding components of the associated  $\lambda_0$  vector. The final demonstration of the consistency between the discrete adjoint fields and the theoretical form of the continuous adjoint solution upwind the shock wave, is obtained by performing a line extraction of the three terms in

$$\begin{aligned} \psi(x, y) = & \phi_\alpha(x \sin(\alpha) - y \cos(\alpha)) \lambda_0^\alpha \\ & + \phi_{\alpha-\mu}(x \sin(\alpha - \mu) - y \cos(\alpha - \mu)) \lambda_0^{\alpha-\mu} \\ & + \phi_{\alpha+\mu}(x \sin(\alpha + \mu) - y \cos(\alpha + \mu)) \lambda_0^{\alpha+\mu}, \end{aligned} \quad (44)$$

and propagating these values in the complete zone upwind the detached shock wave. More precisely the values of these terms are extracted from a fine discrete adjoint field at a distance  $2.3c$  from the leading edge (where the three bands are separated). They are then interpolated everywhere upwind the shock wave according the local values of  $x \sin(\alpha) - y \cos(\alpha)$ ,  $x \sin(\alpha - \mu) - y \cos(\alpha - \mu)$  and  $x \sin(\alpha + \mu) - y \cos(\alpha + \mu)$ . For the finer meshes, the resulting field appears to be visually identical to the actual discrete adjoint field, just upwind of the shock wave, where the bands are superimposed (results not shown here).

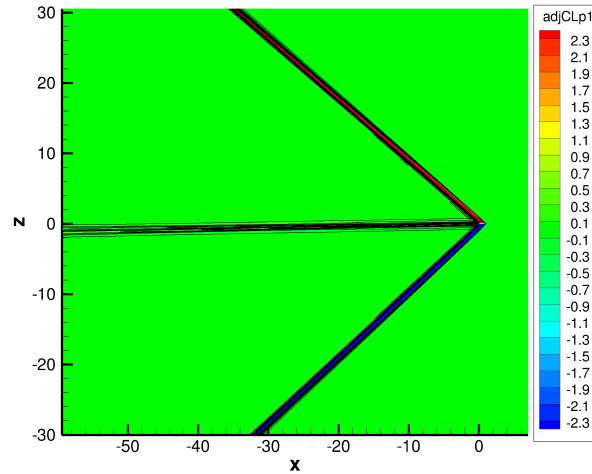


Figure 7: ( $M_\infty = 1.5$ ,  $\alpha = 1^\circ$ ,  $4097 \times 4097$  mesh) Farfield view of first component of  $CL_p$  adjoint.

### 6.1.3. Residual perturbation analysis

If the residual perturbation is located in a supersonic zone, its influence on the flow close to the source appears to be restricted to the downstream part of the streamline and of the two characteristic curves passing by the source location. Moreover, assuming a constant flow  $W$ , by the same arguments as in previous section, its perturbation  $\delta W$  can be expressed as

$$\begin{aligned}\delta W(x, y) = & \quad \psi_{\alpha}(x \sin(\alpha) - y \cos(\alpha))r^{\alpha} \\ & + \quad \psi_{\alpha-\mu}(x \sin(\alpha - \mu) - y \cos(\alpha - \mu))r^{\alpha-\mu} \\ & + \quad \psi_{\alpha+\mu}(x \sin(\alpha + \mu) - y \cos(\alpha + \mu))r^{\alpha+\mu},\end{aligned}\tag{45}$$

where  $\psi_{\gamma}$  stands for a small perturbation scalar function and each  $r^{\gamma}$  vector is a right eigenvector of the Jacobian  $\sin(\gamma)A - \cos(\gamma)B$ . The consistency of the actual numerical  $\delta W$  with this analytical model can be simply assessed, upwind the detached shock, for  $\delta R^1$  and  $\delta R^2$ , since they activate the Mach-lines part of the solution,

$$\psi_{\alpha-\mu}(x \sin(\alpha - \mu) - y \cos(\alpha - \mu))r^{\alpha-\mu} + \psi_{\alpha+\mu}(x \sin(\alpha + \mu) - y \cos(\alpha + \mu))r^{\alpha+\mu},$$

with one-dimensional vector spaces  $\text{span}\{r^{\alpha-\mu}\}$  and  $\text{span}\{r^{\alpha+\mu}\}$ : it was successfully verified that the ratio of the components of the numerical  $\delta W^1$  and  $\delta W^2$  is the one of the corresponding right eigenvector (results not shown here).

On the contrary, if the source term is located in the subsonic bubble or if one of the three curves enters the subsonic bubble, then the support of flow perturbation includes this complete subsonic area consistently with the elliptic nature of the equations [58, chap. 11].

More details are given for the case when the source term is located in the supersonic zone. Let consider the perturbation decomposition (45). If the entropy or the total enthalpy (that are convected in steady state Euler flows) are perturbed ( $\delta R^3$  or  $\delta R^4$ ), close to the source, the perturbation is located along the trajectory downstream the source and possibly along shock waves for  $\delta R^4$ . If these quantities are not altered by the perturbation ( $\delta R^1$  or  $\delta R^2$ ), the response of the steady state flow to the perturbation, close to the source, is located along the two characteristic lines downwind the source and the usual relative-variations along trajectories of thermodynamic and kinetic variables are valid between nominal and locally perturbed flow. More precisely <sup>1</sup>:

- $\delta R^1$  induces no change in the stagnation quantities and entropy. Mach number is decreased along the two characteristic lines starting from the perturbation location. The static pressure, temperature and density are increased and velocity components are also perturbed along these two lines with a decrease of velocity magnitude;
- $\delta R^2$  induces no change in the stagnation quantities and entropy. Along the upper characteristic curve starting from the perturbation point, the static pressure, density, temperature are increased whereas Mach number, velocity magnitude, x-component of velocity are decreased. Opposite variations are observed along the lower characteristic curve. The y-component of the velocity is increased along both characteristic curves;
- $\delta R^3$  induces no variation of stagnation pressure, static pressure and Mach number. An increase of total enthalpy (stagnation temperature), temperature, both components of velocity and entropy is observed along the trajectory starting from the perturbation location. The density is decreased;
- $\delta R^4$  induces no local variation of the static pressure except along shock waves and no variation of the total enthalpy. Mach number, density, stagnation pressure, stagnation density, and both velocity components are increased along the trajectory starting from the perturbation location. Entropy and temperature are decreased along the trajectory. As mentioned end of § 3.3 this notion of perturbation downstream the source and along a streamtube of the initial is only a main order description as the streamtubes structure of a non-constant flow is perturbed by a  $\delta R^4$  source.

---

<sup>1</sup>all variations are given for a positive  $\varepsilon$  in equation (13) and positive components of velocity for the nominal flow

These zones of influence and dependance of the lift and the drag explain in particular the aspect of the discrete adjoint fields close to the trailing edge, that are bounded by the two characteristics curves passing through the trailing edge as seen in Fig. 8. They are also illustrated in Fig. 4(right) presenting the  $\delta W^1$  perturbation on the pressure field plotted together with the characteristic curves passing by the source location.

#### 6.1.4. Adjoint fields across the shock

The adjoint variables are continuous across shocks, whereas their derivatives may be discontinuous [36, 1, 38]. In Fig. 8, a clear discontinuity of the adjoint-drag or the adjoint-lift gradient is observed for the adjoint component associated to  $z$ -coordinate momentum equation.

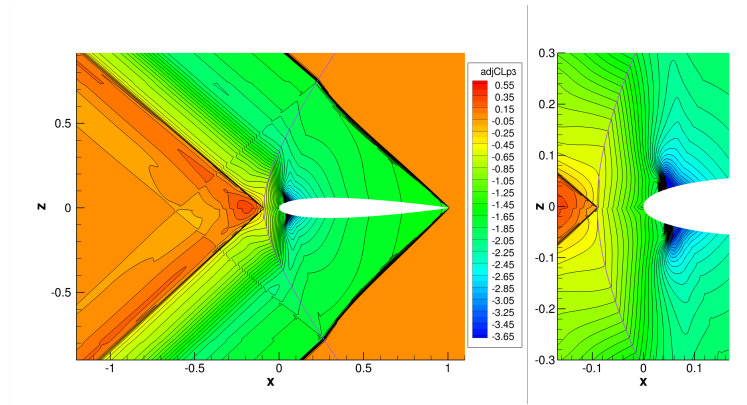


Figure 8: ( $M_\infty = 1.5$ ,  $\alpha = 1^\circ$ ,  $4097 \times 4097$  mesh) Contours of the adjoint component associated to  $z$ -coordinate momentum equation. The position of the shock is indicated by a pink line.

Figure 9 validates the adjoint RH jump relations (39) to (41b) derived in § 5. We here display both lift and drag adjoint solutions. The shock location is about  $s = 0.11$  and we observe that the adjoint RH relations are well satisfied, while the normal gradients of the adjoint variables display large discontinuities at the shock position.

## 6.2. Transonic regime

### 6.2.1. Flow solution

We now consider a transonic flow around the NACA0012 airfoil with conditions  $M_\infty = 0.85$  and  $\alpha = 2^\circ$ . A strong shock wave develops on the suction side and a weaker shock on the pressure side (see Fig. 10).

### 6.2.2. Lift and drag adjoint solutions

Figure A.27 presents the contours of all four components of the drag and lift adjoint fields. (As indicated before, the choice of the scale for the contours of first and last adjoint components in Figs. A.26, A.27 and A.28 allows to visually check that equation (16) is closely satisfied by the discrete adjoint fields.) Both fields exhibit strong values and gradients close to the wall, the stagnation streamline, the two characteristics impinging the upper side and lower shock foot and two other characteristic curves that form a circumflex with the previous two. These features have been observed previously [8, 42, 39, 38].

The physical point of view of Giles and Pierce [1] recalled in § 3.3 is again considered and the  $\delta CL_p^d$  terms corresponding to the four source terms in (13) are plotted in Figs. 10 (right) and A.20. We observe that  $\delta R^1$  and  $\delta R^2$  have a strong impact on  $CL_p$  when located along the characteristic curves that form the two circumflex.  $\delta R^4$  has a strong impact when it is located close to the wall or to the stagnation streamline. The asset of this approach is obvious when studying the singular behavior of the adjoint fields: the  $\delta J^d$  responses to the physical source terms exhibit only part of the singular zones of the classical adjoint fields and the high values/gradients of one  $\delta J^d$  are transferred to all or to several of the usual adjoint components according to equation (15).

The residual of the continuous adjoint equation is calculated as detailed in § 6.1.1. As the mesh is refined, the zones with significant residual have a decreasing area but remain large. Increasing values are also observed close to

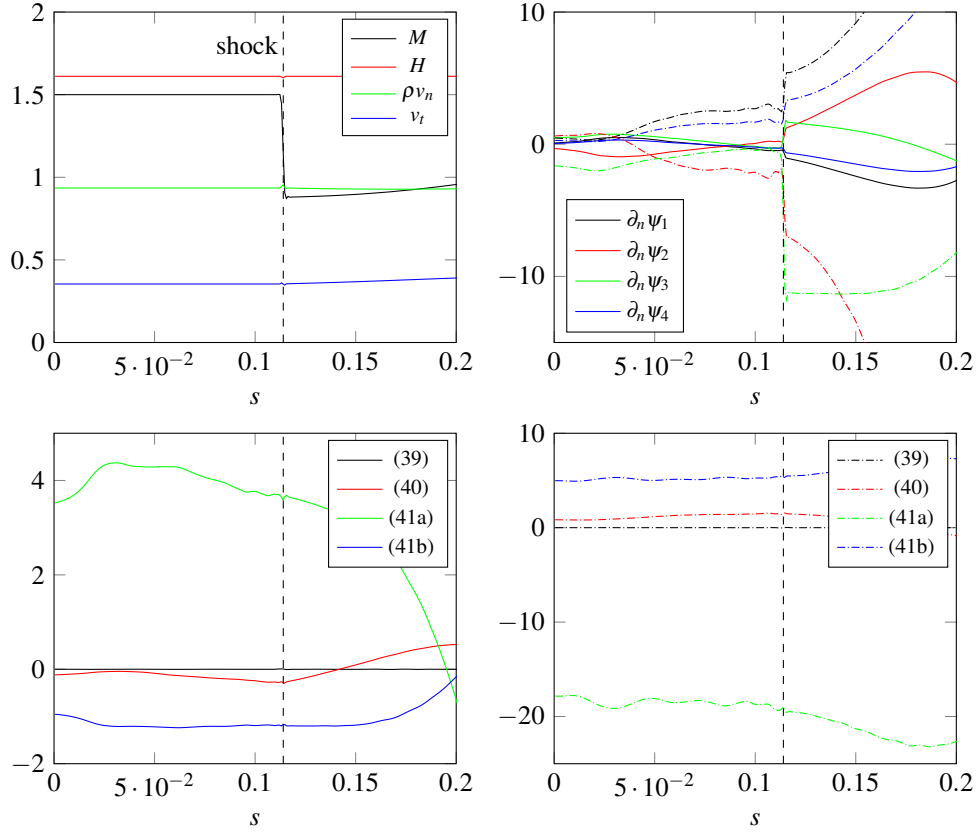


Figure 9: ( $M_\infty = 1.5$ ,  $\alpha = 1^\circ$ ,  $4097 \times 4097$  mesh) Evolutions of direct and drag (continuous lines) and lift (dash-dotted lines) adjoint quantities across the upstream shock between points  $(-0.151, 0.266)$  and  $(0.077, 0.184)$  as a function of the local coordinate  $s$ . An equation number refers to the arguments between brackets  $[[\cdot]]$  in the corresponding equation, e.g.,  $v_n(\partial_n \psi_1 - H \partial_n \psi_4)$  has been plotted for (39).

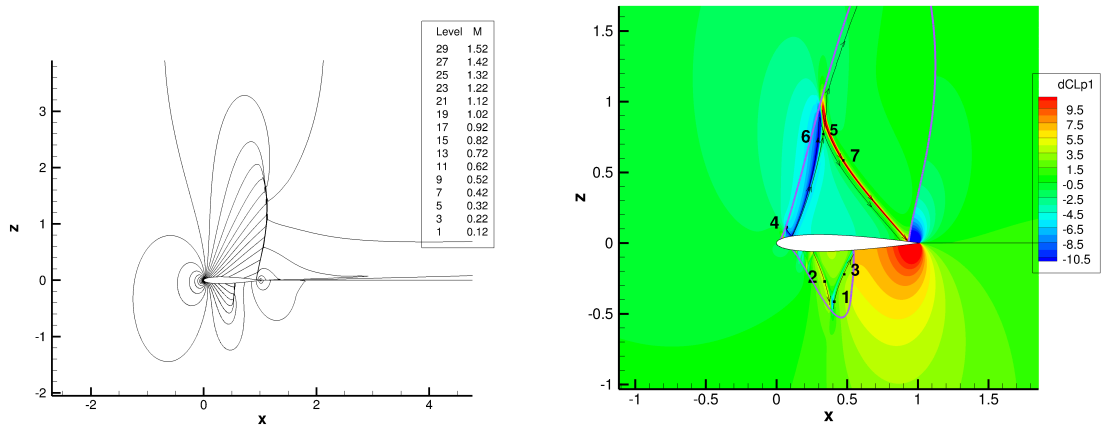


Figure 10: ( $M_\infty = 0.85$ ,  $\alpha = 2^\circ$ ,  $2049 \times 2049$  mesh) Left: contours of Mach number, right: isolines of  $\delta CL_p^1$  (equations (13) and (14) with  $\epsilon=1$ ), location of the points for the residual perturbation analysis plus sonic line (in pink).

the wall, the stagnation streamline and the characteristic line that impacts the upper side shock foot, that are known to be zones of large values and large gradients for the lift and drag adjoints [42, 39, 38] as highlighted in the left part of Fig. 11. The farfield adjoint boundary condition is satisfied by the discrete adjoint fields as the adjoint field is almost zero at the farfield boundary. Right part of Fig. 11 illustrates the verification of continuous-like adjoint wall boundary condition. It is observed that (36) is satisfied except at the shock feet and the trailing edge where the differences in neighboring  $\lambda$  terms are most probably too large for a simple main-order in space analysis.

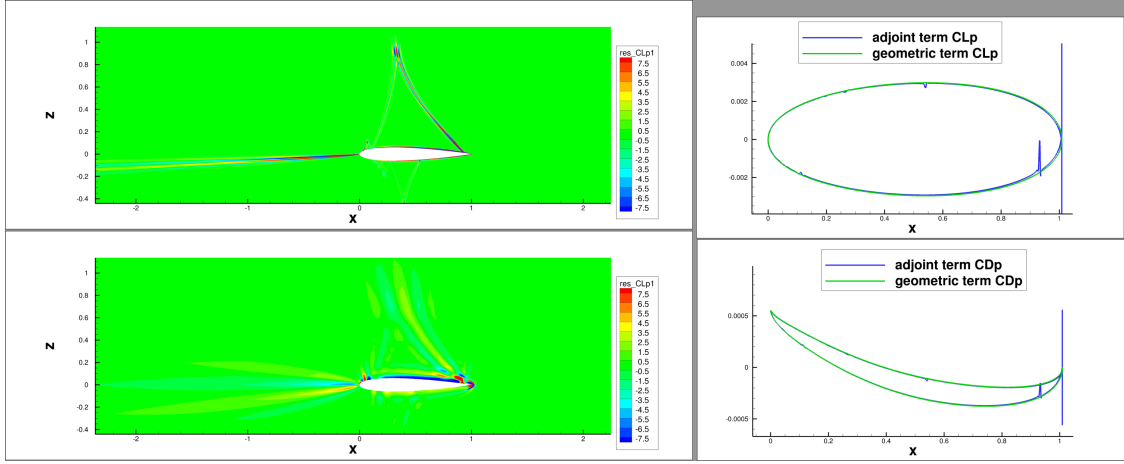


Figure 11: ( $M_\infty = 0.85$ ,  $\alpha = 2^\circ$ ) Left: residual of the continuous equation (first component) evaluated with the lift discrete adjoint fields (bottom:  $129 \times 129$  mesh, top:  $2049 \times 2049$  mesh). Right: geometric and adjoint terms of (36) for lift and drag ( $2049 \times 2049$  mesh).

Figure 12 highlights a clear discontinuity across the shock of the gradient of the drag or the lift adjoint component associated to  $z$ -coordinate momentum. This is further analyzed in Fig. 13 where the lift and drag adjoint derivatives are plotted along a line crossing the shock. Again it is observed that the adjoint RH relations (39) to (41b) are well satisfied, while the normal adjoint derivatives may be discontinuous across the shock.

### 6.2.3. Analysis of $\delta R^1$ and $\delta R^2$ perturbations along specific characteristic lines

The first order variation of  $CL_p$  and  $CD_p$  in response to the physical  $\delta R$  perturbations in (13) and (11) are calculated and plotted for  $CL_p$  in Figs. 10 (right) and A.20. More precisely, we set  $\varepsilon = 1$  in (13) and the intensity of  $\delta J$  is calculated through (11) and affected in the plot to the source location.

The  $\delta R^1$  and  $\delta R^2$  sources, lead to  $\delta CL_p^1$  and  $\delta CL_p^2$  (respectively  $\delta CD_p^1$  and  $\delta CD_p^2$ ) exhibiting strong (positive and negative) values along characteristic lines of the supersonic areas upwind both shocks, in particular along the characteristic lines impacting the shock feet. For a better understanding, the flow perturbation and the lift perturbation  $\delta CL_p^1$  due to the  $\delta R^1$  source terms are calculated for sources located in the upper side supersonic bubble at points 4, 5, 6 and 7 (see Fig. 10). The changes in the wall pressure field (of the re-converged flow) due to  $\delta R^1$  source terms are illustrated in Fig. 14. From the discussion in § 6.1.3, it is known that a positive pressure increment is propagated along the two Mach lines starting from the source location. Its influence at the wall is observed along with the one of other more global perturbations in the flow propagated through the subsonic zones: for a source term located at point 4, there is a visible local increase (and oscillation) of the pressure at about  $x = 0.11$  where the lower characteristic passing by point 4 reaches the wall. Nevertheless, the change in  $CL_p$  is mainly due to global variations of the static pressure all along the airfoil. For point 6, the change in  $CL_p$  is due to the displacement of the lower-side shock and the variation in pressure where the lower characteristic passing at point 6 impacts the wall (small bump at  $x \simeq 0.78$ , upper side, in Fig. 14). Concerning point 7, the change in  $CL_p$  is due to the displacement of both, the upper side and the lower side shock. Point 5 has been placed close to point 6 and 7 in order to better understand why a point close to the two well-marked characteristic curves may have a weak influence on  $CL_p$  and  $CD_p$ . Actually, for this point, the influence of the upper side shock displacement and the lower characteristic impact (small bump at  $x \simeq 0.87$ , at the upper side, in Fig. 14) almost vanishes. This is the reason for the corresponding low  $\delta CL_p^1$  value.

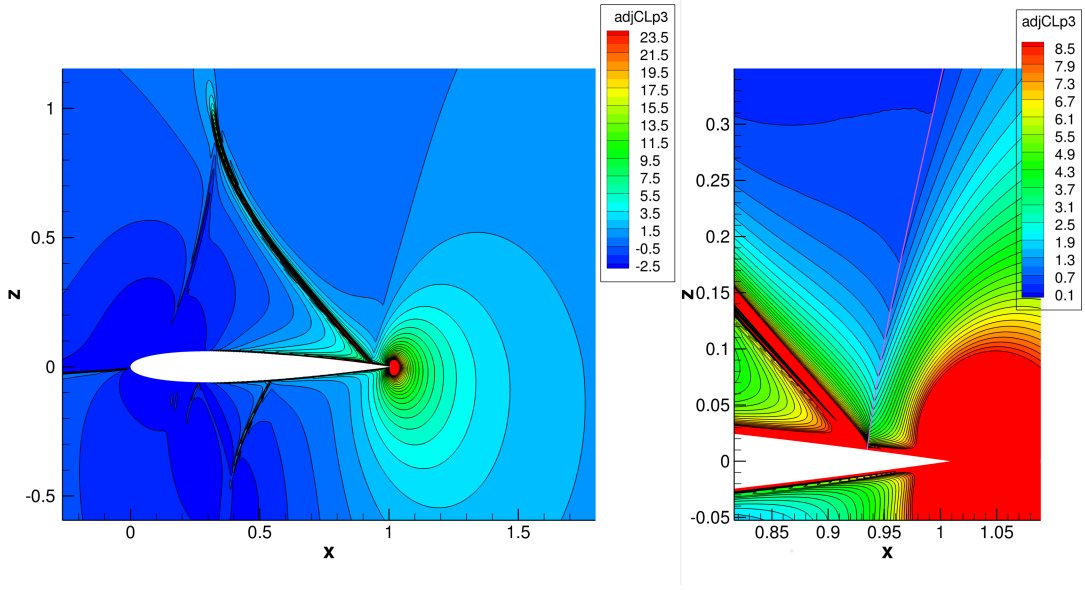


Figure 12: ( $M_\infty = 0.85$ ,  $\alpha = 2^\circ$ ,  $4097 \times 4097$  mesh) Contours of adjoint component associated to  $z$ -coordinate momentum equation (sonic line in pink).

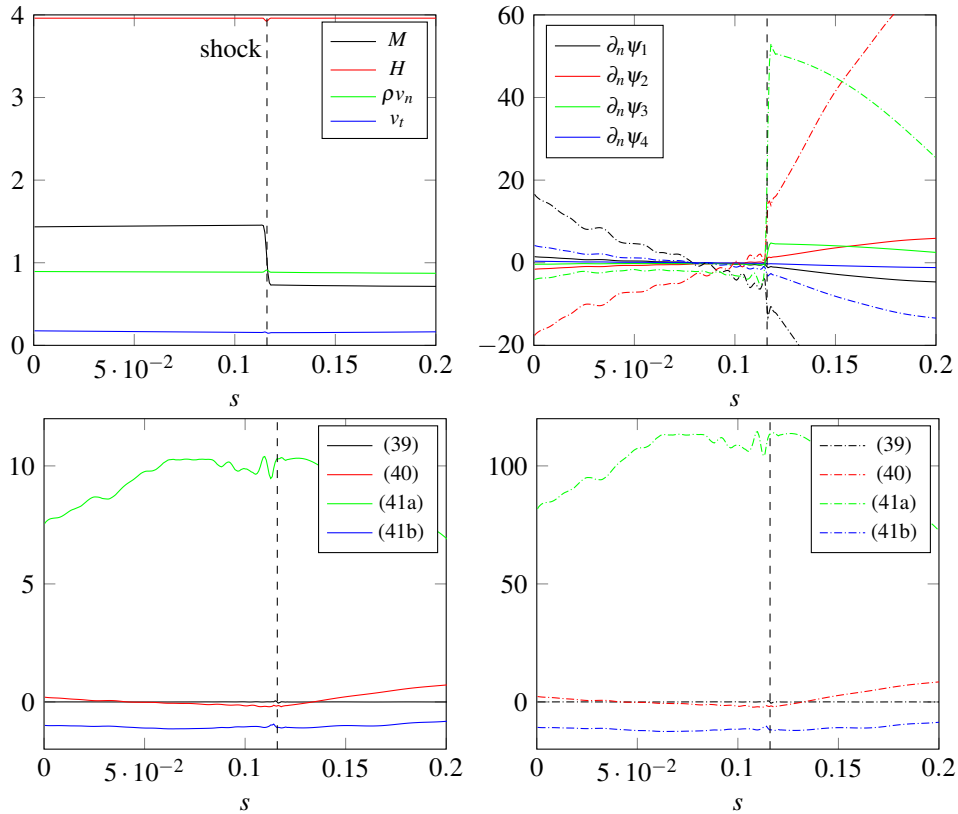


Figure 13: ( $M_\infty = 0.85$ ,  $\alpha = 2^\circ$ ,  $4097 \times 4097$  mesh) Evolutions of direct and drag (continuous lines) and lift (dash-dotted lines) adjoint quantities across the upper shock between points  $(0.865, 0.064)$  and  $(1.016, 0.038)$  as a function of the local coordinate  $s$ . An equation number refers to the arguments between brackets  $[[\cdot]]$  in the corresponding equation, e.g.,  $v_n(\partial_n \psi_1 - H \partial_n \psi_4)$  has been plotted for (39).

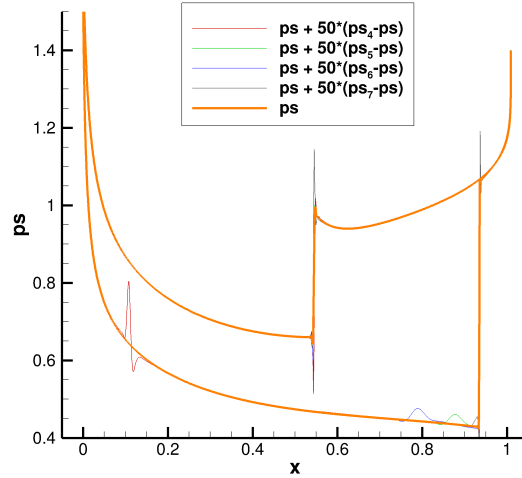


Figure 14: ( $M_\infty = 0.85$ ,  $\alpha = 2^\circ$ ,  $2049 \times 2049$  mesh) Pressure distribution at the wall. Influence of  $\delta R^1$  (equation (13) with  $\varepsilon = 6.e^{-6}$ ) source terms located at points 5, 6, 7 and 8 (variation w.r.t. nominal flow 50 times amplified)

#### 6.2.4. Analysis of $\delta R^4$ perturbation in the vicinity of the wall and the stagnation streamline

As mentioned beforehand observing Fig. A.20,  $\delta R^4$  is the physical source term responsible for high values of lift/drag-adjoint and gradient of adjoint close to the wall and the stagnation streamline. The mechanism by which  $\delta R^4$  modifies the flow field and the forces values is detailed for the vicinity of the stagnation streamline and the wall upper side.

In the first series of considered perturbed flows, the  $\delta R^4$  source terms are located upper side, in the supersonic area, along a mesh line orthogonal to the wall, close to  $x = 0.5$ . In a supersonic zone, the perturbation of the flow caused by a  $\delta R^4$  source term along the corresponding streamline has been described in section § 6.1.3. Actually, at large scale, the pressure field is not altered except by the displacement of the two shocks and the upper side shock position of the nominal flow is not compatible with the increased upwind Mach number (ie for this almost normal shock, the classical equation for the ratio of downwind over upwind static pressure as a function of the upwind Mach number can not be satisfied where the perturbed streamline hits the shock). In fact, the upper side shock is moved globally backwards and the shifted shock goes with a decreased upwind static pressure and an increased downwind static pressure (see local slopes of the orange curve in Fig. 14). It is observed that the smaller the distance of the source and perturbed streamline to the wall, the larger the displacement of the upper side shock foot which explains the growth of  $\delta CLp^4$  in the vicinity of the wall. Observing the static pressure changes at smaller scales, it is noted, as expected, that the perturbation of the static pressure in the subsonic area is not restricted to the continuation of the streamline but extends to the whole subsonic area close to the profile downstream the shocks. As concerning the static pressure close to the lower side, at these finer scales, an increase is observed upwind the shock and below the trailing edge whereas a decrease is observed downwind the shock; this goes with a backward displacement of the lower shock. This is illustrated in Fig. 15 (left). Both changes of the static pressure at the wall correspond to an increase of the lift that is consistent with the local values of  $\delta CLp^4$ .

If the  $\delta R^4$  source is located close to the wall but downwind the upper side shock, similar shock displacements and lower side fine scale perturbations of the pressure are observed. On the contrary, the flow perturbations created downwind the upper side shock are very different for sources located on the same streamline either sides of the shock.

Concerning the points located close to the stagnation streamline, the mechanism that produces the lift perturbation  $\delta CLp^4$  due to the  $\delta R^4$  source, seems to be correlated with particles convection since the iso- $\delta CLp^4$  roughly follow the streamlines (see Fig. A.20 right). Independently of the equations specific to supersonic flows or supersonic bubbles in

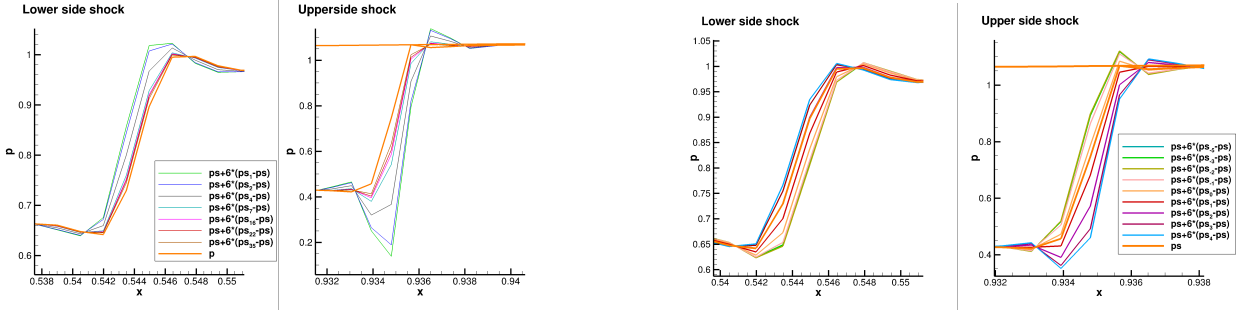


Figure 15: ( $M_\infty = 0.85$ ,  $\alpha = 2^\circ$ ,  $2049 \times 2049$  mesh) Left: Influence of  $\delta R^4$  source terms located close to the wall on shocks position (source at points  $(1536, j)$   $j = 1, 2, 4, 7, 22, 35$ ) – right: Influence of  $\delta R^4$  source terms located close to the stagnation streamline on shocks position (source at points  $(1010 + l, 433)$   $l = -5, -3, -2, -1, 0, 1, 2, 3, 4$ )

transonic flows that have been used before, let us first note that the base transonic flow satisfies everywhere  $dp_0/dt = 0$  (due to homogeneous farfield state and absence of source-term).  $\delta R^4$  is obtained by the partial derivation of the inviscid flux in the flow direction with respect to the stagnation pressure, at constant total enthalpy and static pressure and, from a fluid dynamics point of view, the expected main order perturbation (see end of §3.3) of the stagnation pressure field is the convection of the local increment created by the source downwind the source location. For a numerical point of view, a dissipated propagation of the  $\delta p_0$  from the source location is observed (see Fig. A.24 that also illustrates the propagation of the decrease of entropy created by the source). After this increment has been propagated up to the upper side shock, the mechanism through which both shocks are moved is the same as the one described before. The perturbation of the pressure distribution is illustrated in Fig. 15 (right) for a series of sources located close to the stagnation streamline, about  $0.6c$  upwind the stagnation point.

In [1], the authors consider a 2D inviscid flow about an airfoil and an output  $J$  defined as the integral along the wall of the pressure times a local factor. With the additional approximation of potential flow, they then derive the asymptotic behavior of  $\delta J_m^4$ , the variation of  $J$  under  $\delta R^4$ , when the source term is located in the vicinity of the stagnation streamline. Subject to this assumption, they prove that  $\delta J^4 \simeq \pm d^{-1/2}$  where  $d$  is the distance of the source  $m$  to the stagnation streamline and the sign is changed when crossing the streamline. This relation is not always numerically well satisfied by numerical lift / drag adjoint fields of Euler flows [39, 38]. For the transonic test-case of interest, it has been demonstrated above that  $\delta CL p_m^4$  and  $\delta CD p_m^4$  result in similar perturbations of the flow for points  $m$  located on the same streamline, close to the stagnation streamline and close to the wall upwind the shock. As the considered meshes are structured and essentially orthogonal at each vertex (in particular at the wall) [54], it is easy to search for the  $\gamma$  exponent such that  $\delta J^4 \simeq d^\gamma$  in the vicinity of the wall. For our numerical solutions, this exponent appears to depend on the  $x$  location (rather than on  $CD$  vs  $CL$ , lower side vs upper side or mesh density). It is decreasing with increasing  $x$ , from 0. at the leading edge to about -0.1 at  $x = 0.8$  and then more rapidly when moving closer to the trailing edge.

Just as for stagnation pressure, the main order perturbation of the stagnation density field and the entropy field is also a dissipated convection of the increment created at the source. The Crocco equation for an inviscid flow with uniform total enthalpy reads  $V \wedge (\nabla \times V) = -T \nabla s$  and results in the following perturbation equation

$$\delta(V) \wedge (\nabla \times V) + V \wedge \delta(\nabla \times V) = -\delta(T \nabla s), \quad (46)$$

that appears to be well satisfied by numerical solutions (see e.g. Fig. A.25). As recent articles discussed the singularity of lift and drag adjoint at the trailing edge, as  $\delta R^4$  is the physical source term responsible for high values / high gradient of adjoint at the wall, we finally note that the perturbed Crocco equation is singular at the trailing edge (and more generally along the trailing edge slip line): it is the only location where the  $\delta(V) \wedge (\nabla \times V)$  term is not negligible with respect to  $V \wedge \delta(\nabla \times V)$  which may enter the discussion about the singularity of lift/drag adjoint at the trailing edge.



### 6.3. Subsonic regime

Finally, we consider a smooth subsonic flow with freestream conditions  $M_\infty = 0.4$  and  $\alpha = 5^\circ$ . The Mach number contours are presented in Fig. 16 where we observe the stagnation point located just under the leading edge as well as a strong acceleration of the flow on the upper side due to the profile incidence.

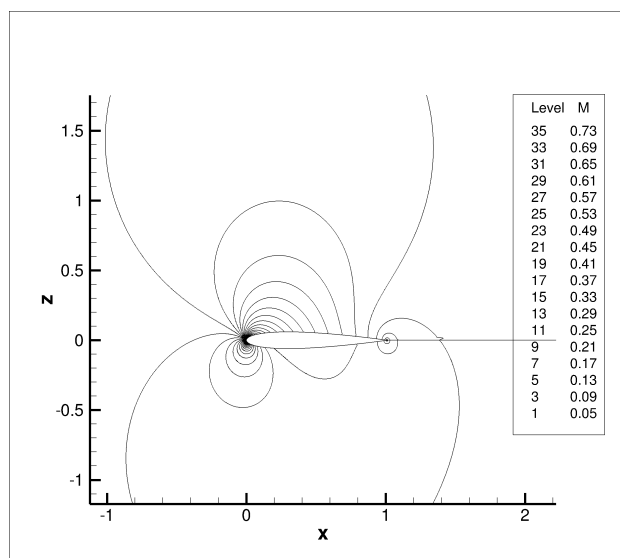


Figure 16: ( $M_\infty = 0.4$ ,  $\alpha = 5^\circ$ ,  $2049 \times 2049$  mesh) Mach number contours.

#### 6.3.1. Lift and drag adjoint solutions

Figure A.28 presents the contours of all four components of the adjoint fields. The lift adjoint components exhibit strong values and gradients close to the wall and the stagnation streamline. The amplitudes of these values increase as the mesh is refined. Conversely, all components of the drag adjoint appear to be bounded and mesh converging. These different behaviors may be attributed to the facts that the adjoint field quantifies the sensitivity of the quantity of interest w.r.t. the residuals, and that the limit inviscid drag is zero for a subsonic flow whereas the limit lift is not.

The residuals of the continuous adjoint equations have been calculated as detailed in § 6.1.1. As the mesh is refined, the zones with significant residuals for the lift-adjoint have a decreasing support but exhibit increasing values close to the wall and to the stagnation streamline (see left part of Fig. 17). The farfield adjoint boundary condition is satisfied by the discrete adjoint fields as the adjoint field is almost zero at the farfield boundary. Right part of Fig. 17 shows that the adjoint wall boundary condition (36) is well satisfied for both lift and drag.

The physical point of view of Giles and Pierce [1] is then considered to gain understanding for the behavior of the lift-adjoint<sup>2</sup>. The  $\delta CLp^1$ ,  $\delta CLp^2$ ,  $\delta CLp^3$ , and  $\delta CLp^4$  responses have been calculated and plotted in Fig. A.21. We observe that  $\delta R^4$  is the only source responsible for the singular behavior of the adjoint-lift close to the wall and stagnation streamline.

#### 6.3.2. Residual perturbation analysis in the vicinity of wall and stagnation streamline

As for transonic or supersonic flows, a  $\delta R^4$  source results in positive increments of the stagnation pressure and the stagnation density and a negative increment of entropy, and all three increments are convected downstream the source location following the classical laws for Euler flows with uniform total enthalpy. However, the response of the

<sup>2</sup>let us briefly note that this approach is somehow making the analysis more complex for this flow condition when applied to the drag. Actually, the numerical solutions exhibit  $dCD^4$  values such that  $dCD^4 \rightarrow -\infty$  in the vicinity of the stagnation point (see right subplot of Fig. A.22) but note that all terms of the last line of the matrix in equation (15) vanish. This finally results in bounded and mesh converging adjoint components for drag

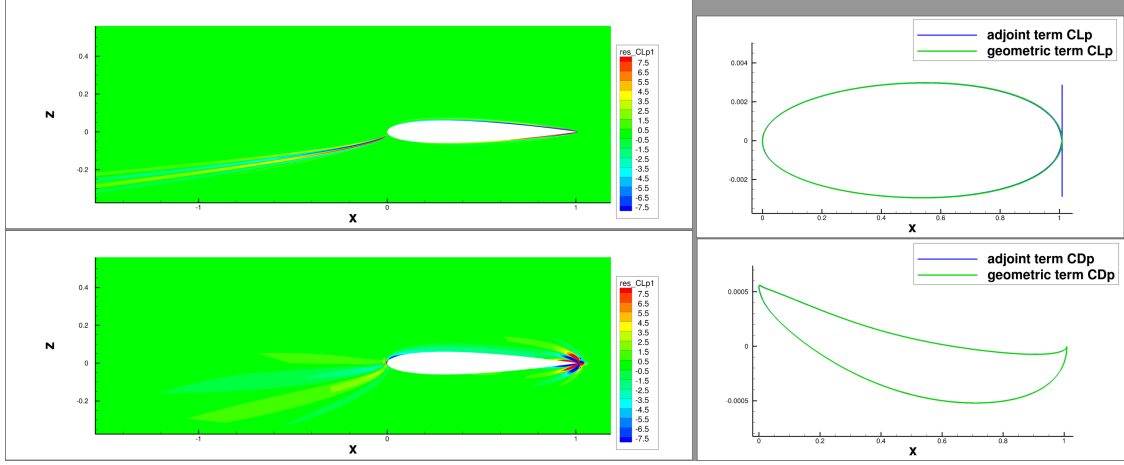


Figure 17: ( $M_\infty = 0.4$ ,  $\alpha = 5^\circ$ ) Left: residual of the continuous equation (first component) evaluated with the lift discrete adjoint fields (down  $129 \times 129$  mesh, up  $2049 \times 2049$  mesh). Right: geometric and adjoint terms of equation (36) for lift and drag ( $2049 \times 2049$  mesh).

subsonic flow to the local perturbation of these three quantities, is very different from the one described in § 6.2.4 for the selected transonic flow: density, velocity, static pressure, Mach number and all derived variables exhibit a global perturbation (see Fig. A.24). When the source is located close to stagnation streamline, the perturbation is the strongest close to the leading edge. If it is located just under (resp. above) the stagnation streamline, the main effect on the static pressure at the wall is a decrease all along the pressure (resp. suction) side consistently with the local sign of  $\delta CLp_4$  (Fig. A.21 right and Fig. 18).

As in the transonic case, we examine whether  $\delta CLp^4 \simeq d^\gamma$  in the vicinity of the wall. Once again, a negative  $\gamma$  exponent decreasing from 0 to about -0.20 with increasing  $x$  is derived from this assumption – see Fig. A.23 right.

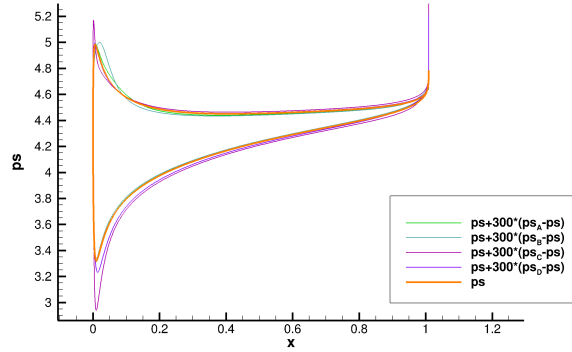


Figure 18: ( $M_\infty = 0.4$ ,  $\alpha = 5^\circ$ ,  $2049 \times 2049$  mesh) Pressure at the wall. Influence of  $\delta R^4$  source term located at points A, B, C, D, on the static pressure at the wall. Distance of points A, B, C, D to the leading edge  $\simeq 0.6$ . Respective distance to stagnation line is 0.0400, 0.0187 (trajectory to lower side), 0.0181, 0.397 (trajectory to upper side)

## 7. Conclusion

In this work, we address open issues in the field of discrete and continuous adjoint equations for inviscid flows. The results are illustrated through in-depth numerical experiments on lift- and drag-adjoint fields for inviscid flows

about the NACA0012 airfoil in supersonic, transonic and subsonic regimes.

We first investigate the dual consistency of the JST scheme in cell-centered FV formulation for the discretization of the compressible Euler equations in 2D. We prove dual consistency of the scheme at interior cells, while inconsistency occurs at the penultimate cell to a physical boundary due to the absence of artificial dissipation at the boundary. We hence propose a slight modification of the exact scheme derivation w.r.t. the penultimate-cell flow variables to recover consistency. The implementation of this modification is straightforward and was shown to improve the convergence of the adjoint computation at wall boundaries under grid refinement. The modification has been carried out in our code and successfully illustrated. The link between continuous inviscid adjoint boundary condition at the wall and cell-centered discrete adjoint equation in the cell adjacent to the wall has also been established.

Second, a new heuristic method has been proposed to discuss the adjoint consistency of discrete adjoint fields. It consists in discretizing the continuous equation with the discrete flow and discrete-adjoint field and discuss the convergence of the residual towards zero as the mesh is refined. Coherently with the demonstrated property of adjoint consistency, this residual has been found to be vanishing except in areas where: (a) a discontinuous adjoint field is expected (typically, vicinity of the trailing edge for supersonic flows); (b) the discrete adjoint field exhibits increasing values and gradients and where theoretical divergence is suspected (stagnation streamline, wall, specific characteristic lines in supersonic areas).

Third, we derive the general adjoint Rankine-Hugoniot relations across a shock and give relations linking the normal derivatives across the shock. These relations have been numerically validated for a supersonic and a transonic flow. Besides, as the studied shockwave of the transonic flow is almost normal, the presented results answer questions recently raised about the adjoint gradient at shockwaves [38].

We then use these tools for the analysis of the adjoint fields and in particular the analysis of the zones where increasing values and gradients of lift/drag adjoint are observed about profiles, at some flow conditions, when the mesh is refined [1, 39, 38, 59]. The novelty in this domain is both, to take a detailed benefit of the source term approach of Giles and Pierce [1] identifying the  $\delta R$  source term(s) associated to the known zones of numerical divergence, and to consider some corresponding shifted flows  $W + \delta W$  (resulting of the  $\delta R$  source) to understand the fluid dynamics mechanisms that provoke strong changes in lift and drag. The focus has been put on the  $\delta R^4$  source that appears to be associated with the high values and gradients of the discrete adjoints, that are observed at many transonic flow conditions, close to the wall and to the stagnation streamline. This  $\delta R^4$  source actually results in the convection of an increment of stagnation pressure, stagnation density and entropy (provoking shock displacement) at globally constant total enthalpy and locally constant static pressure. Many properties of transonic flows lift or drag adjoint fields are clarified by this approach: it first unifies the behavior expected at the wall and stagnation streamline. It also explains the difference of numerical behavior in lift or drag adjoint at high transonic Mach numbers (shock-wave feet at trailing edge, no possible shock-foot displacement, no adjoint numerical divergence) and lower transonic Mach numbers (more upwind shock-wave feet locations, shock feet displacement under the influence of  $\delta R^4$ , adjoint numerical divergence). Besides, this approach provides a mechanical counterpart to the mathematical study of the lift and drag adjoint asymptotic behavior in the vicinity of the wall and stagnation streamline at the flow conditions for which numerical divergence is observed.

Future work will concern the extension of this analysis to laminar flows considering the usual FV cell-centered discretizations of the viscous flux.

## Acknowledgments

The authors express their warm gratitude to J.C. Vassberg and A. Jameson for allowing the co-workers of D. Destarac to use their hierarchy of O-grids around the NACA0012 airfoil.

This research did not receive any specific grant from funding agencies in the public, commercial or not-for-profit sector

## Bibliography

### References

- [1] Giles, M. and Pierce, N. Adjoint equations in CFD: Duality, boundary conditions and solution behaviour. In *AIAA Paper Series, Paper 97-1850*. (1997).
- [2] Frank, P. and Shubin, G. A comparison of optimisation based approaches for a model computational aerodynamics design problem. *Journal of Computational Physics* **98**, 74–89 (1992).
- [3] Pironneau, O. On optimum design in fluid mechanics. *J. Fluid Mech.* **64**(1), 97–110 (1974).
- [4] Jameson, A. Aerodynamic design via control theory. *Journal of Scientific Computing* **3**(3), 233–260 (1988).
- [5] Jameson, A., Martinelli, L., and Pierce, N. Optimum aerodynamic design using the Navier-Stokes equations. *Theoretical and Computational Fluid Dynamics* **10**(1), 213–237 (1998).
- [6] Castro, C., Lozano, C., Palacios, F., and ZuaZua, E. Adjoint approach to viscous aerodynamic design on unstructured grids. *AIAA Journal* **45**(9), 2125–2139 (2007).
- [7] Becker, R. and Rannacher, R. An optimal control approach to a posteriori error estimation in finite element methods. *Acta Numerica* **10**, 1–102 (2001).
- [8] Venditti, D. and Darmofal, D. Grid adaptation for functional outputs: Application to two-dimensional inviscid flows. *Journal of Computational Physics* **176**, 40–69 (2002).
- [9] Dwight, R. Heuristic *a posteriori* estimation of error due to dissipation in finite volume schemes and application to mesh adaptation. *Journal of Computational Physics* **227**, 2845–2863 (2008).
- [10] Loseille, A., Dervieux, A., and Alauzet, F. Fully anisotropic mesh adaptation for 3D steady Euler equations. *Journal of Computational Physics* **229**, 2866–2897 (2010).
- [11] Fidkowski, K. and Roe, P. An entropy approach to mesh refinement. *SIAM Journal of Scientific Computing* **32**(3), 1261–1287 (2010).
- [12] Fidkowski, K. and Darmofal, D. Aerodynamic design optimization on unstructured meshes using the Navier-Stokes equations. *AIAA Journal* **49**(4), 673–694 (2011).
- [13] Peter, J., Nguyen-Dinh, M., and Trontin, P. Goal-oriented mesh adaptation using total derivative of aerodynamic functions with respect to mesh coordinates – with application to Euler flows. *Computers and Fluids* **66**, 194–214 (2012).
- [14] Belme, A., Alauzet, F., and Dervieux, A. An a priori anisotropic goal-oriented error estimate for viscous compressible flow and application to mesh adaptation. *Journal of Computational Physics* **376**, 1051–1088 (2019).
- [15] Lions, J. L. *Contrôle optimal de systèmes gouvernés par des équations aux dérivées partielles*. Etudes mathématiques. Paris: Dunod, Gauthier-Villars, (1968).
- [16] Sartor, F., Mettot, C., and Sipp, D. Stability, receptivity, and sensitivity analyses of buffeting transonic flow over a profile. *AIAA Journal* **53**(7), 1980–1993 (2015).
- [17] Morris, M., Mitchell, T., and Ylvisaker, D. Bayesian design and analysis of computer experiments: Use of derivatives in surface prediction. *Technometrics* **35**(3), 243–255 (1993).
- [18] Luchini, P. and Bottaro, A. Adjoint equations in stability analysis. *Annu. Rev. Fluid Mech.* **46**(1), 493–517 (2014).
- [19] Talagrand, O. and Courtier, P. Variational assimilation of meteorological observations with the adjoint vorticity equation. I: Theory. *Q. J. R. Meteorol. Soc.* **113**(478), 1311–1328 (1987).
- [20] Anderson, W. and Bonhaus, D. Airfoil design optimization on unstructured grids for turbulent flows. *AIAA Journal* **37**(2), 185–191 (1999).
- [21] Nielsen, E. and Anderson, W. Aerodynamic design optimization on unstructured meshes using the Navier-Stokes equations. *AIAA Journal* **37**(11), 185–191 (1999).
- [22] Nemec, N. and Zingg, D. Newton–Krylov algorithm for aerodynamic design using the Navier–Stokes equations. *AIAA Journal* **40**(6), 1146–1154 (2002).
- [23] Xu, S., Radford, D., M., M., and J.-D., M. Stabilisation of discrete steady adjoint solvers. *Journal of Computational Physics* **299**, 175–195 (2015).
- [24] Giles, M., Duta, M., and Müller, J.-D. Adjoint code developments using the exact discrete approach. In *AIAA Paper Series, Paper 2001-2596*. (2001).
- [25] Lu, J. and Darmofal, D. Adaptive precision methodology for flow optimisation via discretization and iteration error control. In *AIAA Paper Series, Paper 2004-1996*. (2004).
- [26] Hartmann, R. Adjoint consistency analysis of discontinuous Galerkin discretizations. *SIAM J. Numer. Anal.* **45**(6), 2671–2696 (2007).
- [27] Shi, L. and Wang, Z. Adjoint-based error estimation and mesh adaptation for the correction procedure via reconstruction method. *Journal of Computational Physics* **295**, 261 – 284 (2015).
- [28] Duivesteijn, G., Bijl, H., Koren, B., and van Brummelen, E. On the adjoint solution of the quasi-1D Euler equations: the effect of boundary conditions and the numerical flux function. *International Journal for Numerical Methods in Fluids* **47**, 987–993 (2005).
- [29] Lozano, C. A note on the dual consistency of the discrete adjoint quasi-one dimensional Euler equations with cell-centred and cell-vertex central discretization. *Computers and Fluids* **134-135**, 51–60 (2016).
- [30] Liu, Z. and Sandu, A. On the properties of the discrete adjoints of numerical methods for the advection equation. *International Journal for Numerical Methods in Fluids* **56**, 769–803 (2008).
- [31] Hicken, J. and Zingg, D. Dual consistency and functional accuracy: a finite-difference perspective. *Journal of Computational Physics* **256**, 161–182 (2014).
- [32] Stück, A. An adjoint view on flux consistency and strong wall boundary conditions to the Navier-Stokes equations. *Journal of Computational Physics* **301**, 247–264 (2015).
- [33] Stück, A. Dual-consistency study for Green-Gauss gradient schemes in an unstructured Navier-Stokes method. *Journal of Computational Physics* **350**, 530–549 (2017).
- [34] Majda, A. The stability of multidimensional shock fronts. In *Memoirs of the AMS*, 275. Amer. Math. Soc., (1983).

- [35] Ulbrich, S. A sensitivity and adjoint calculus for discontinuous solutions of hyperbolic conservation laws with source terms. *SIAM J. Control Optim.* **41**(3), 740–797 (2002).
- [36] Giles, M. B. and Pierce, N. A. Analytic adjoint solutions for the quasi-one-dimensional euler equations. *J. Fluid Mech.* **426**, 327–345 (2001).
- [37] Baeza, A., Castro, C., Palacios, F., and Zuazua, E. 2d Euler shape design on non-regular flows using adjoint Rankine-Hugoniot relations. *AIAA Journal* **47**(3), 552–562 (2009).
- [38] Lozano, C. Singular and discontinuous solutions of the adjoint Euler equations. *AIAA Journal* **56**(11), 4437–4451 (2018).
- [39] Lozano, C. On the properties of the solutions of the 2D adjoint Euler equations. In *Proceedings of EUROGEN 2017, Madrid*, (2017).
- [40] Lozano, C. Watch your adjoints! lack of mesh convergence in inviscid adjoint solutions. *AIAA Journal* **56**(11), 4437–4451 (2018).
- [41] Giles, M. and Pierce, N. Improved lift and drag estimates using adjoint Euler equations. In *AIAA Paper Series, Paper 99-3293*. (1999).
- [42] Todarello, G., Vonck, F., Bourasseau, S., Peter, J., and Désidéri, J.-A. Finite-volume goal-oriented mesh-adaptation using functional derivative with respect to nodal coordinates. *Journal of Computational Physics* **313**, 799–819 (2016).
- [43] Jameson, A., Schmidt, W., and Turkel, E. Numerical solutions of the Euler equations by finite volume methods using Runge-Kutta time-stepping schemes. In *AIAA Paper Series, Paper 1981-1259*. (1981).
- [44] Giles, M. and Pierce, N. An introduction to the adjoint approach to design. *Flow, Turbulence, Combustion* **65**, 393–415 (2000).
- [45] Anderson, W. and Venkatakrisnan, V. Aerodynamic design optimization on unstructured grids with a continuous adjoint formulation. *Computers and Fluids* **28**, 443–480 (1999).
- [46] Hiernaux, S. and Essers, J.-A. An optimal control theory based algorithm to solve 2D aerodynamic shape optimisation problems for inviscid and viscous flows. In *Proceedings of the RTO-AVT Symposium on Aerodynamic Design and Optimisation of Flight Vehicles*, (1999).
- [47] Hiernaux, S. and Hessers, J.-A. Aerodynamic optimization using Navier-Stokes equations and optimal control theory. In *AIAA Paper Series, Paper 99-3297*. (1999).
- [48] Peter, J. and Dwight, R. Numerical sensitivity analysis for aerodynamic optimization: a survey of approaches. *Computers and Fluids* **39**, 373–391 (2010).
- [49] Hirsch, C. *Numerical Computation of Internal and External Flows: The Fundamentals of Computational Fluid Dynamics (second edition)*. Butterworth – Heineman. Elsevier, (2007).
- [50] Goodman, J. and Majda, A. The validity of the modified equation for nonlinear shock waves. *J. Comput. Phys.* **58**(3), 336 – 348 (1985).
- [51] Giles, M. and Pierce, N. An introduction to the adjoint approach to design. In *Proceedings of ERCOFTAC Workshop on Adjoint Methods*, (1999).
- [52] Nguyen-Dinh, M. *Qualification des simulations numériques par adaptation anisotropique de maillages*. PhD thesis, Université de Nice-Sophia Antipolis, March (2014).
- [53] Dwight, R. and Brezillon, J. Effect of approximations of the discrete adjoint on gradient-based optimization. *AIAA Journal* **44**(12), 3022–3031 (2006).
- [54] Vassberg, J. and Jameson, A. In pursuit of grid convergence for two-dimensional Euler solutions. *Journal of Aircraft* **47**(4), 1152–1166 (2010).
- [55] Cambier, L., Heib, S., and Plot, S. The elsA CFD software: input from research and feedback from industry. *Mechanics & Industry* **14**(3), 159–174 (2013).
- [56] Destarac, D. Far-field / near-field drag balance and applications of drag extraction in cfd, February (2003).
- [57] Peter, J., Renac, F., Dumont, A., and Méheut, M. Discrete adjoint method for shape optimization and mesh adaptation in the elsA code. status and challenges. In *Proceedings of 50th 3AF Symposium on Applied Aerodynamics, Toulouse*, (2015).
- [58] Anderson, J. *Modern Compressible Flow (third edition)*. McGraw-Hill, (2003).
- [59] Peter, J., Labbé, C., and Renac, F. Analysis of discrete adjoint fields for 2d Euler flows. In *Proceedings of eurogen 2019. ECCOMAS*, (2019).

## Appendix A. Additional figures

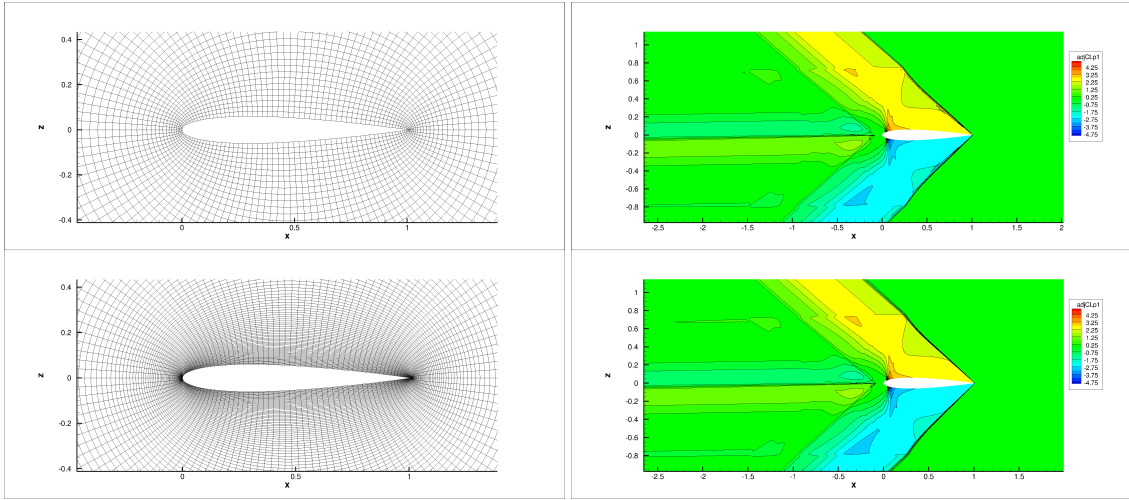


Figure A.19: ( $M_\infty = 1.5$ ,  $\alpha = 1^\circ$ ) Close view of the two  $2049 \times 2049$  meshes (view of coarse extracted meshes with the same skip) and corresponding first component of lift adjoint.

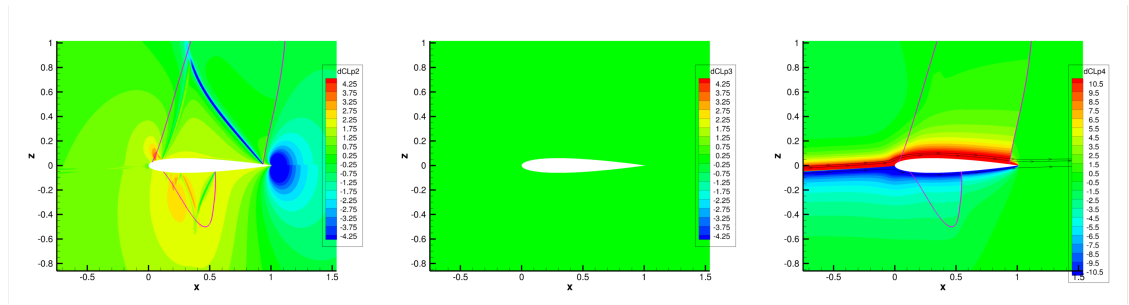


Figure A.20: ( $M_\infty = 0.85$ ,  $\alpha = 2^\circ$ ,  $2049 \times 2049$  mesh) Left: contours of  $\delta CL_p^2$ ,  $\delta CL_p^3$ ,  $\delta CL_p^4$  (equations (13) and equation (14) with  $\varepsilon=1$ ).

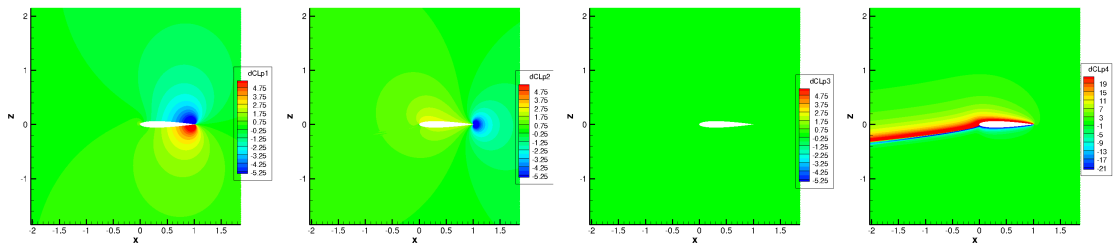


Figure A.21: ( $M_\infty = 0.4$ ,  $\alpha = 5^\circ$ ,  $2049 \times 2049$  mesh) Contours of  $\delta CL_p^1$ ,  $\delta CL_p^2$ ,  $\delta CL_p^3$ ,  $\delta CL_p^4$  (equations (13) and equation (14) with  $\varepsilon=1$ ).

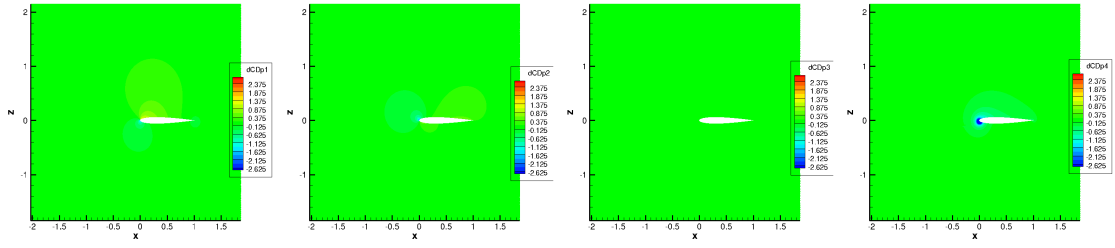


Figure A.22: ( $M_\infty = 0.4$ ,  $\alpha = 5^\circ$ ,  $2049 \times 2049$  mesh) Contours of  $\delta CD_p^1$ ,  $\delta CD_p^2$ ,  $\delta CD_p^3$ ,  $\delta CD_p^4$  (equations (13) and (14) with  $\varepsilon=1$ ).

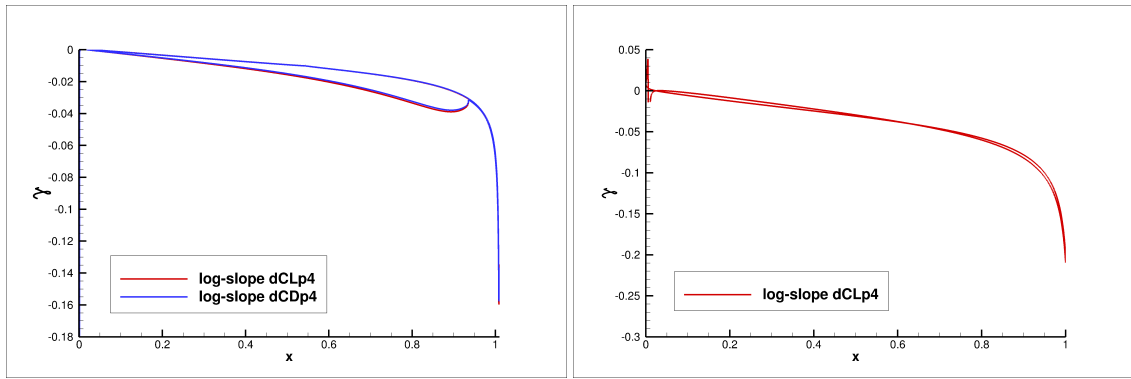


Figure A.23: ( $4097 \times 4097$  mesh) Estimation of the exponent for  $\delta CL_p^4 \simeq d^{\gamma}$  based of three last rows of cells adjacent to the wall. Left:  $M_\infty = 0.85$ ,  $\alpha = 2^\circ$ , right:  $M_\infty = 0.4$ ,  $\alpha = 5^\circ$ .

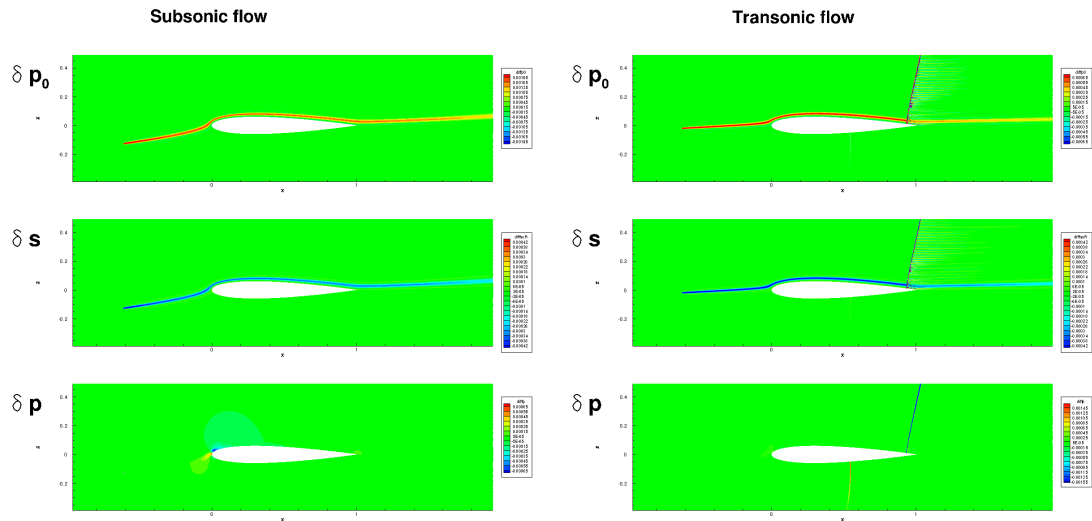


Figure A.24: ( $2049 \times 2049$  mesh) Difference in stagnation pressure, entropy (divided by perfect gas constant) and static pressure w.r.t. nominal flow due to  $\delta R^4$ . Left:  $M_\infty = 0.4$ ,  $\alpha = 5^\circ$ , source in  $(-0.612, -0.127)$ . Right:  $M_\infty = 0.85$ ,  $\alpha = 2^\circ$ , source in  $(-0.623, -0.020)$

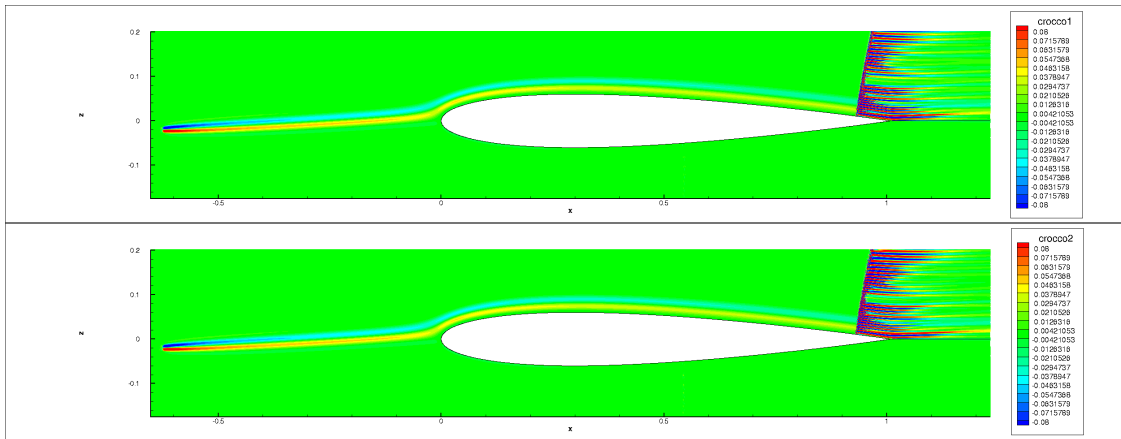


Figure A.25: ( $M_\infty = 0.85$ ,  $\alpha = 2^\circ$ ,  $2049 \times 2049$  mesh)  $\delta R^4$  source term at point  $(-0.62, -0.02)$ . Discretization of left- and right-hand-side of perturbed Crocco equation (46) ( $z$  component).



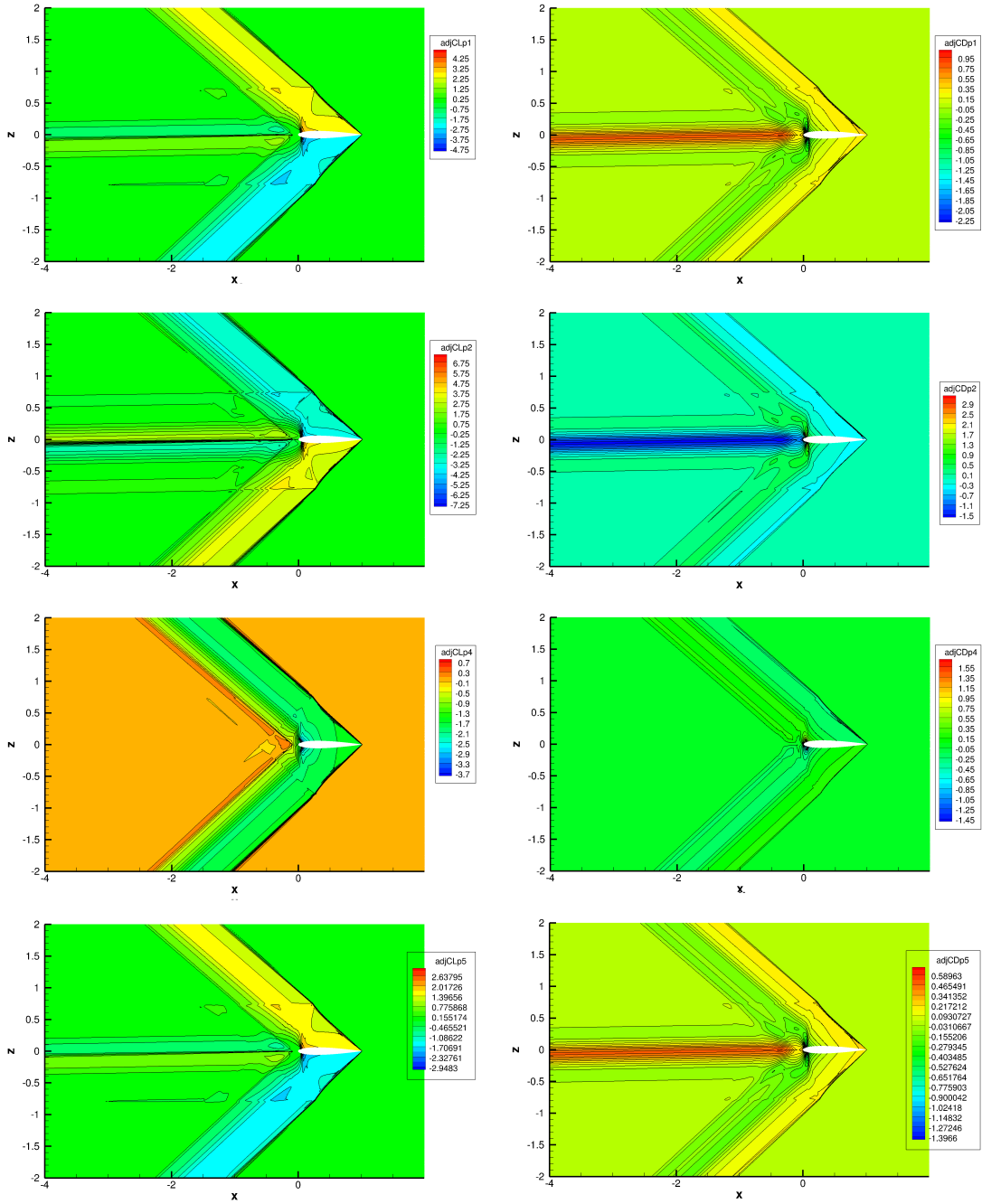


Figure A.26: ( $M_\infty = 1.5$ ,  $\alpha = 1^\circ$ ,  $2049 \times 2049$  mesh) Left: lift adjoint, right: drag adjoint.

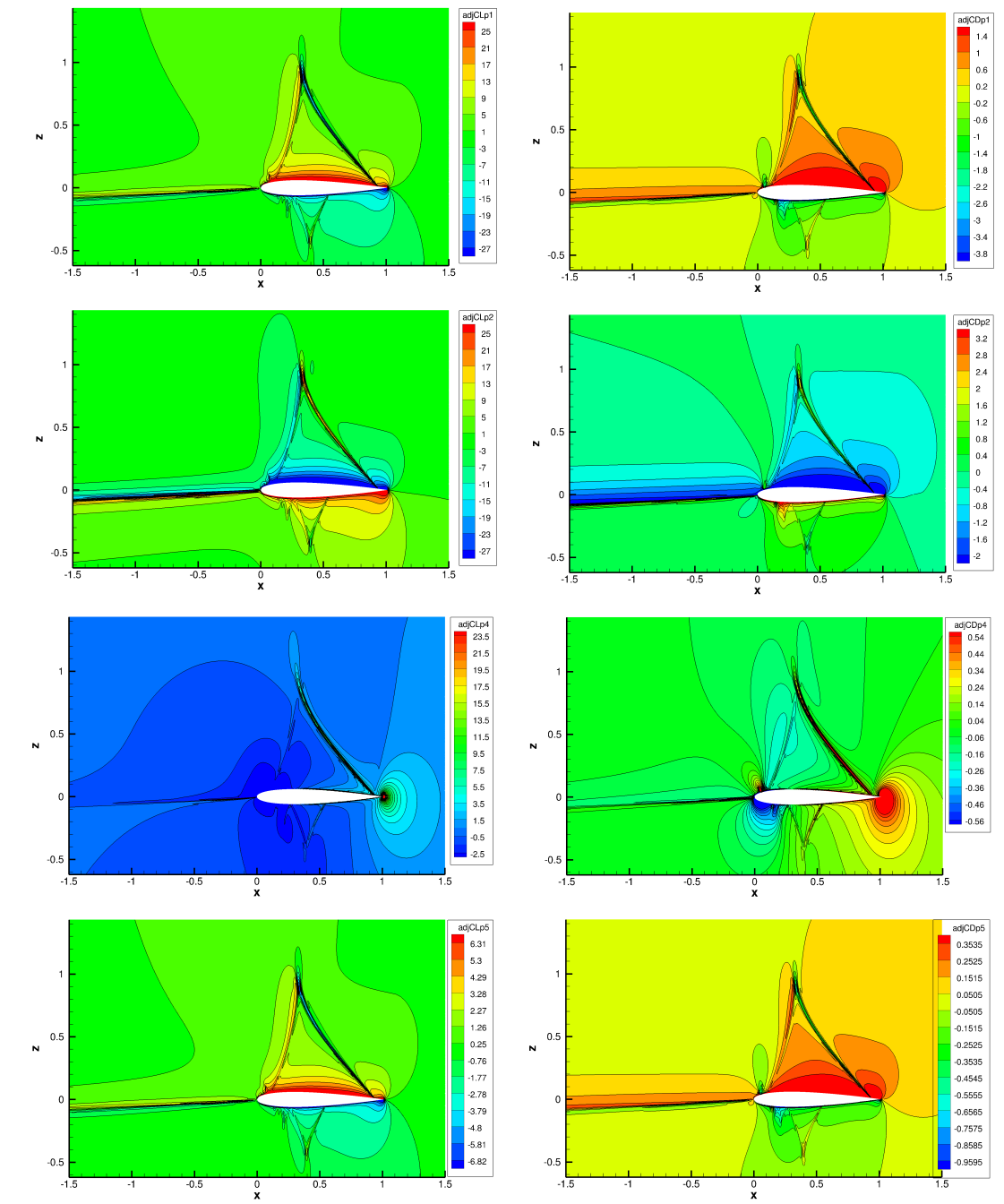


Figure A.27: ( $M_\infty = 0.85$ ,  $\alpha = 2^\circ$ ,  $2049 \times 2049$  mesh) Left: lift adjoint, right: drag adjoint.

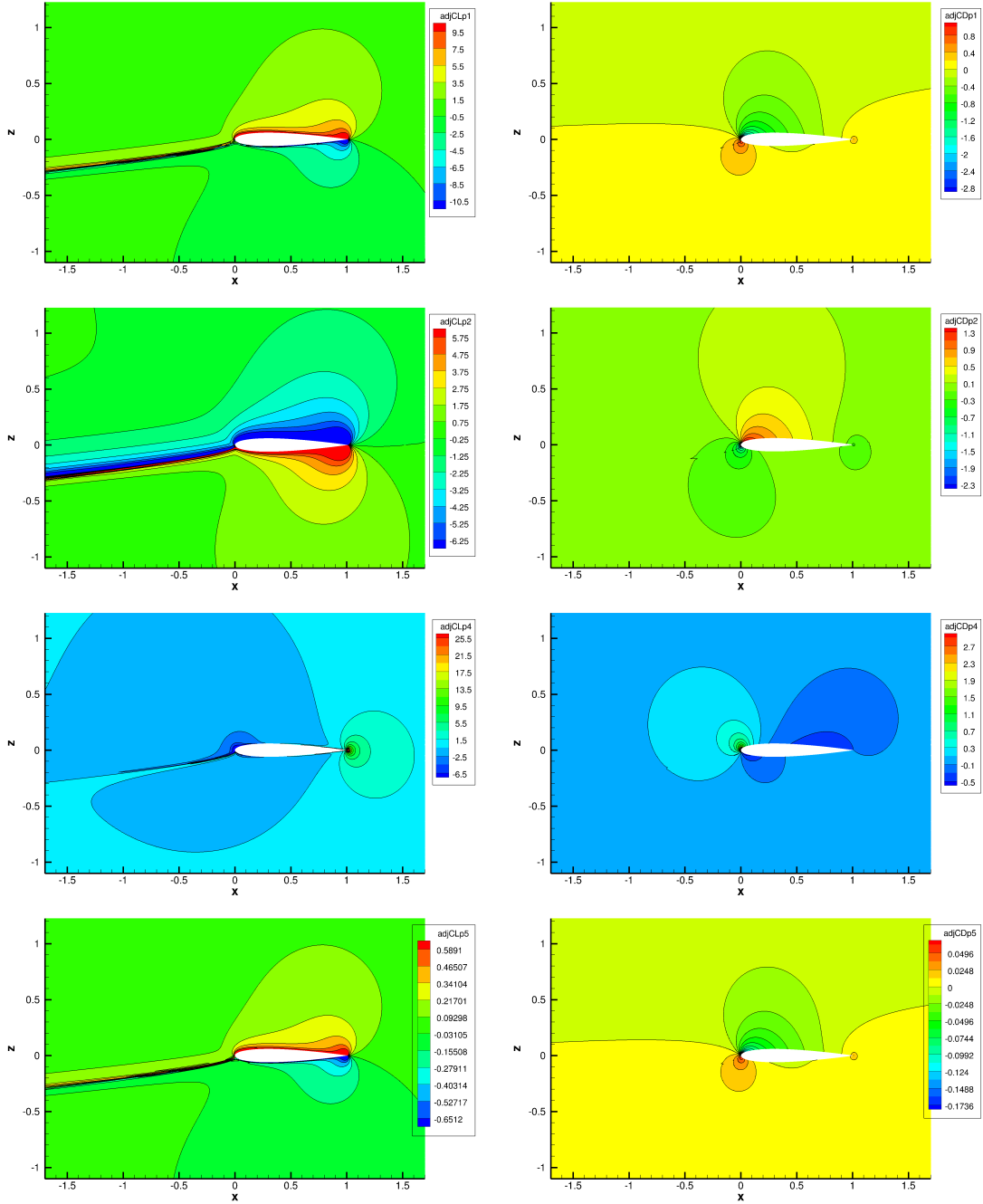


Figure A.28: ( $M_\infty = 0.4$ ,  $\alpha = 5^\circ$ ,  $2049 \times 2049$  mesh) Left: lift adjoint, right: drag adjoint.